communications biology

Article

https://doi.org/10.1038/s42003-024-06955-3

Metabolic regulation of mitochondrial morphologies in pancreatic beta cells: coupling of bioenergetics and mitochondrial dynamics

Wen-Wei Tseng[1], Ching-Hsiang Chu[1], Yi-Ju Lee[1], Shirui Zhao[2,3,4,5], Chen Chang[1], Yi-Ping Ho[2,3,4,5] & An-Chi Wei[1,6]

Cellular bioenergetics and mitochondrial dynamics are crucial for the secretion of insulin by pancreatic beta cells in response to elevated levels of blood glucose. To elucidate the interactions between energy production and mitochondrial fission/fusion dynamics, we combine live-cell mitochondria imaging with biophysical-based modeling and graph-based network analysis. The aim is to determine the mechanism that regulates mitochondrial morphology and balances metabolic demands in pancreatic beta cells. A minimalistic differential equation-based model for beta cells is constructed that includes glycolysis, oxidative phosphorylation, calcium dynamics, and fission/fusion dynamics, with ATP synthase flux and proton leak flux as main regulators of mitochondrial dynamics. The model shows that mitochondrial fission occurs in response to hyperglycemia, starvation, ATP synthase inhibition, uncoupling, and diabetic conditions, in which the rate of proton leakage exceeds the rate of mitochondrial ATP synthesis. Under these metabolic challenges, the propensities of tip-to-tip fusion events simulated from the microscopy images of the mitochondrial networks are lower than those in the control group and prevent the formation of mitochondrial networks. The study provides a quantitative framework that couples bioenergetic regulation with mitochondrial dynamics, offering insights into how mitochondria adapt to metabolic challenges.

Mitochondria, which are responsible for the generation of adenosine triphosphate (ATP) via oxidative phosphorylation (OXPHOS), are motile organelles that exhibit dynamic structures owing to fission and fusion cycles[1–6]. Fission-fusion cycles, which are typically referred to as mitochondrial dynamics, are related to the regulation of energy production and the quality control of the mitochondrial network[7–9]. Mitochondrial fusion and biogenesis maintain the mitochondrial mass and network[10–12]. Moreover, quality control is achieved by asymmetric fission, which splits one mitochondrion into two daughter mitochondria with different mitochondrial membrane potentials. Deenergized mitochondria are subsequently removed through mitophagy[4,9,13–15]. At the molecular level, fusion and fission events are driven by large GTPases. Mitofusin 1 (Mfn1) and 2 (Mfn2) on the outer mitochondrial membrane (OMM) and optic atrophy 1 (OPA1) on the inner mitochondrial membrane (IMM) are associated with fusion events. In contrast, mitochondrial fission 1 protein (Fis1), dynamin-related/-like protein 1 (Drp1), and Dynamin2 (Dnm2) regulate mitochondrial fission events[1,12,16–21].

The mitochondrial network may shift to different morphologies depending on the metabolic task. Recent studies have linked the nutrient supply and energy demand to mitochondrial dynamics, which implies that the mitochondrial architecture adapts to metabolic demands[22–26]. Taking rat insulinoma (INS-1) cells as an example[7], mitochondrial networks are more tubular during the G1 to S phases to produce energy and perform biosynthesis, whereas mitochondria are more fragmented during the G2 to M

[1]Graduate Institute of Biomedical Electronics and Bioinformatics, National Taiwan University, Taipei, Taiwan. [2]Department of Biomedical Engineering, The Chinese University of Hong Kong, Shatin, New Territories, Hong Kong SAR, China. [3]Centre for Novel Biomaterials, The Chinese University of Hong Kong, Shatin, New Territories, Hong Kong SAR, China. [4]Hong Kong Branch of the CAS Center for Excellence in Animal Evolution and Genetics, The Chinese University of Hong Kong, Shatin, New Territories, Hong Kong SAR, China. [5]The Ministry of Education Key Laboratory of Regeneration Medicine, Shatin, New Territories, Hong Kong SAR, China. [6]Department of Electrical Engineering, National Taiwan University, Taipei, Taiwan. e-mail: acwei86@ntu.edu.tw

phases to ensure that mitochondria are equally distributed into daughter cells. In cancer cells, mitochondrial dynamics are also crucial for metabolic rewiring, metastasis, drug resistance, and cancer stem cell survival[27–29]. Pancreatic beta cells sense the glucose concentration by coupling glycolysis to the citric acid cycle (CAC) and OXPHOS to synthesize ATP, and this step increases the ATP-to-ADP ratio, closes ATP-inhibited potassium channels (KATP channels), triggers calcium influx, and excretes insulin vesicles[30,31]. This process, which is called glucose-stimulated insulin secretion (GSIS), is correlated with changes in mitochondrial morphology[32–34]. Glucose stimulation can induce short-term (approximately 1 h) mitochondrial fragmentation and recovery[32].

In contrast, perturbations in mitochondrial dynamics are associated with the deterioration of mitochondrial network quality, mitochondrial dysfunction, decreased ATP synthesis capacity, impaired calcium homeostasis, and even cell death[35]. Insulin resistance and type 2 diabetes (T2DM) are associated with hampered mitochondrial functions in OXPHOS and CAC metabolism[36,37], which leads to a decrease in the sensitivity of beta cells to glucose stimulation for the secretion of insulin. Fragmented mitochondrial network morphologies have also been found in diabetic beta cells[25,38–42]. The artificial blockage of fission proteins in INS-1E cells hinders glucose sensing and insulin secretion[32].

A variety of studies have evaluated mitochondrial morphology and mitochondrial network fission/fusion dynamics through various techniques. For instance, researchers can gain direct evidence of mitochondrial network shapes and measure mitochondrial motility, fission, and fusion rates through fluorescence microscopy[43–45]. Image preprocessing and analysis techniques are indispensable for revealing information from these data and further providing quantitative evidence of the results based on mitochondrial dynamics[45–48].

In contrast, in silico models are attained through computer simulations and describe the relationships between substrate input and mitochondrial ATP production. The widely adopted[46–51] mathematical model of beta-cell mitochondria by Magnus and Kaiser[52] described the influence of intracellular calcium dynamics and adenylate levels on ATP synthesis and the mitochondrial membrane potential. The model was further simplified[53] and then revised[54] to reveal the frequency by which ATP synthesis responds to respiring substrates and the cytosolic concentrations of calcium. The INS beta-cell models constructed by Fridlyand et al. [55–58] are focused on ATP production, plasma membrane potential dynamics, intracellular calcium oscillations, signal transduction, and insulin secretion in response to glucose stimulation, i.e. GSIS. Although mitochondrial bioenergetics models describe ATP synthesis upon substrate addition, mitochondria are regarded as a single entity without fission/fusion dynamics.

Alternatively, mitochondria can be treated as individual agents that undergo fission/fusion dynamics, and the overall mitochondrial network mass, structure, and quality can be evaluated[59–61]. Patel and coworkers[35] devised an agent-based model (ABM) to simulate mitochondrial movement, fission, fusion, mitophagy, and biogenesis processes and revealed that the selective mitophagy of damaged mitochondria improves overall mitochondrial health. Sukhorukov and coworkers[62] described mitochondrial fission-fusion dynamics as the dissociation and association of nodes to simulate the images of mitochondrial networks in HeLa cells obtained through fluorescence microscopy. Their idea was further expanded by Zamponi et al. to analyze mitochondrial network structural complexity and Shah et al.[41] to estimate fission/fusion rate differences in healthy and unhealthy cells.

However, only a few studies have combined bioenergetics and mitochondrial fission-fusion dynamics due to the complexity involved in the mathematical model and the scarcity of data related to fusion and fission rates from microscopic observations obtained with microscopes. One of the few examples is Kornick's population-based model[63], which is a minimalistic ODE-based model that simulates the dynamics of fragmented/fused and healthy/unhealthy mitochondrial populations and is dependent on the generation and consumption of ATP. However, the mathematical descriptors for bioenergetics and fission/fusion rates were set based on constant ratios of healthy and unhealthy mitochondria without considering any mechanistic details of OXPHOS and the associated effects on mitochondrial dynamics.

To this end, our study aimed to bridge cellular bioenergetics, mitochondrial network dynamics, and microscopic observations together (Fig. 1). We simulated the model and matched the mitochondrial network pattern changes observed by microscopy under various metabolic

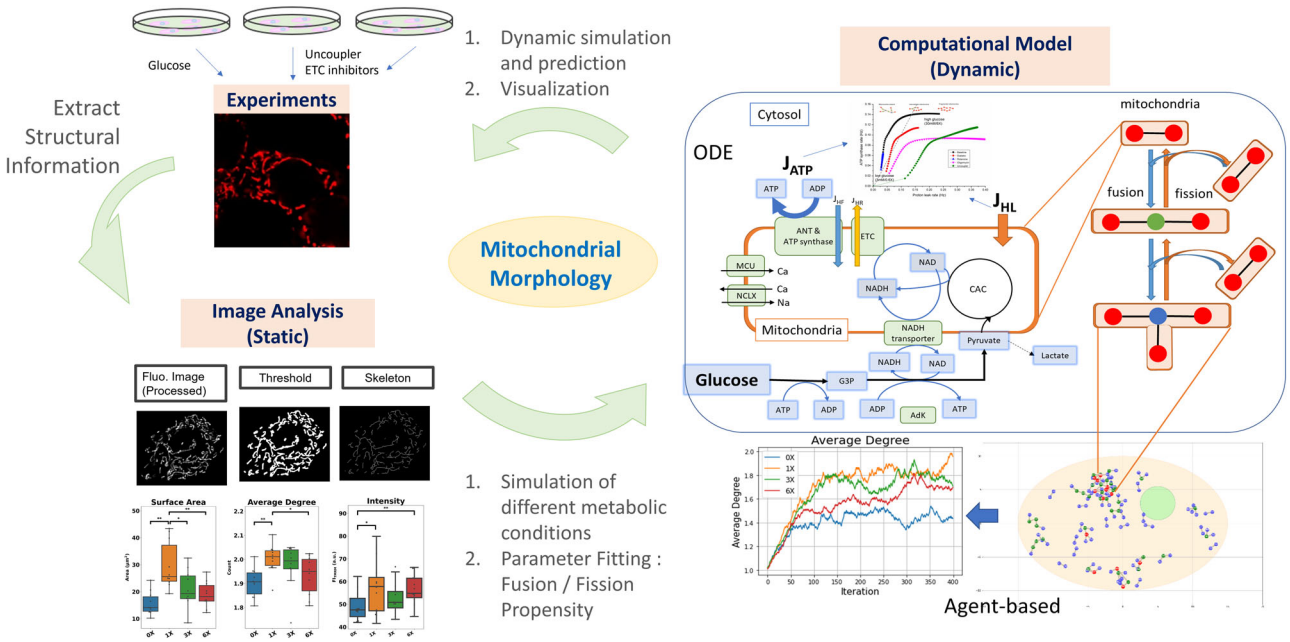

Fig. 1 | Study of mitochondrial bioenergetics and dynamics coupling. Glucose and inhibitors of the mitochondrial respiratory chain induced different mitochondrial responses and morphological changes in INS-1 cells. Image analyses were used to quantify the changes in fluorescence microscopy images of mitochondria under metabolic challenges. Computational models that coupled mitochondrial bioenergetics and mitochondrial dynamics were used to simulate and explain the experimental observations.

conditions, such as different glucose concentrations and in the presence of chemicals that affect the mitochondrial respiratory chain, to investigate the bioenergetic coupling of mitochondrial dynamics in pancreatic beta cells. Model simulations revealed how the mechanisms that regulate mitochondrial dynamics can link the nutrient environment to mitochondrial dynamics and bioenergetics; in addition, the simulations revealed how these mechanisms are related to progressive mitochondrial dysfunction in metabolic diseases.

Results

Interactions between mitochondrial energetics and dynamics

To study the relationship between mitochondrial bioenergetics and mitochondrial dynamics, we varied the ATP synthase capacity to simulate oligomycin blocking ATP synthase, the electron transport chain (ETC) capacity to simulate rotenone blocking respiratory complex I, and the proton leak parameter to simulate carbonyl cyanide-p-trifluoromethoxyphenylhydrazone (FCCP) increasing the proton leak rate. We also varied glucose concentrations simultaneously, creating a two-dimensional map of steady states (Fig. 2). We collected and compared the steady states of the average degree of nodes, the mitochondrial membrane potential, and the ATP-to-ADP ratio. The cell responses to the toxicants were used as a testing set to constrain the model parameters, and glucose and other substrates were used for validation. In all scenarios, when the glucose levels increased, the decreased average degree of nodes tended to cause the mitochondrial network to fragment, and both the ATP-to-ADP ratio and the mitochondrial membrane potential increased. The inhibition of ATP synthase activity resulted in higher mitochondrial membrane potentials, a lower ATP-to-ADP ratio, and a more fragmented mitochondrial network. In contrast, the inhibition of ETC activity moderately suppressed the mitochondrial membrane potential and the ATP-to-ADP ratio and generated a fused mitochondrial network. An increase in proton leak decreased the mitochondrial membrane potential, decreased the ATP-to-ADP ratio, and disrupted the mitochondrial network (Fig. 2). A similar trend in mitochondrial dynamics was also observed in the Mitometer[64] measurements of fission-fusion rates from the time-lapse images of INS-1 cells cultured in different media. (Supplementary Fig. 1b).

Glucose stimulates mitochondrial bioenergetics with morphological changes

We further investigated mitochondrial morphological changes that occurred upon glucose stimulation. Glucose is a stimulus signal for metabolic-secretion coupling. Mitochondria in pancreatic beta-cells respond to increases in blood glucose, which leads to an increased ATP-to-ADP ratio from increased oxidative phosphorylation; then, this process triggers the release of insulin granules from increasing intracellular calcium concentrations. Thus, the first step in determining how cellular metabolism regulates mitochondrial dynamics involves exploring the mechanism through which glucose concentration affects mitochondrial dynamics. We simulated steady-state concentrations of metabolites in response to a range of glucose concentrations. Elevated glucose concentrations increased the steady-state levels of glycolysis metabolites (glyceraldehyde 3-phosphate and pyruvate), the CAC product (NADH), and the OXPHOS products (ATP and ATP-to-ADP ratio) (Fig. 3a–g). Glycolytic flux through glucokinase (GK) drove the downstream reactions between CAC and OXPHOS. The average cytosolic calcium concentration (Fig. 3c) also increased because it was linked to an increasing ATP-to-ADP ratio (Fig. 3f) in this model.

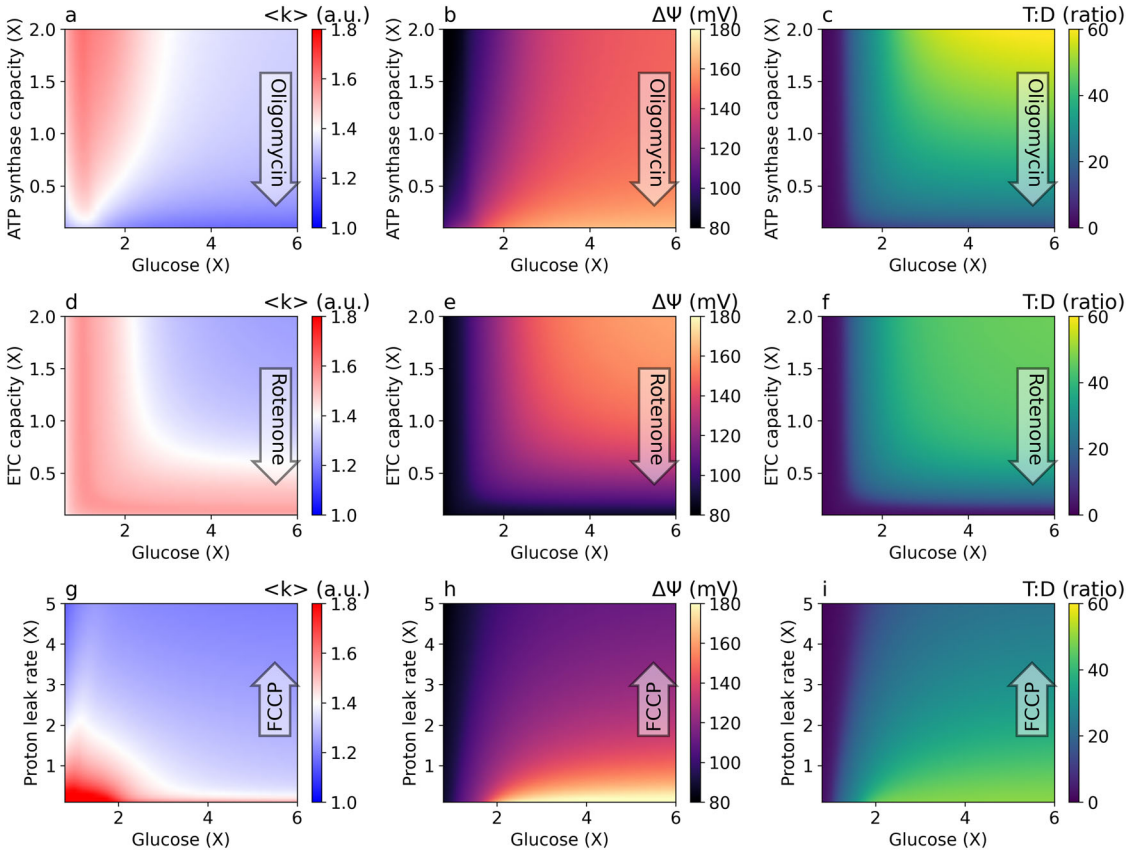

Fig. 2 | Steady-state values for a range of glucose concentrations and mitochondrial bioenergetics. The steady-state values of the average node degree (**a**, **d**, and **g**; denoted as <k >), mitochondrial membrane potential (**b**, **e**, and **h**; denoted as ΔΨ) and ATP-to-ADP ratio (**c**, **f**, and **i**; denoted as T:D) are represented by the colors in the 2D contour plots. The relative glucose concentrations are shown on the X-axis, and 5 mM is denoted as 1X in the simulation. The relative activities of ATP synthase (**a**, **b**, and **c**), the ETC (**d**, **e**, and **f**), and proton leakage activity (**g**, **h**, and **i**) on the Y-axis are presented by comparison to the baseline model values. The translucent arrows indicate how the mitochondrial parameters change in response to the addition of oligomycin, rotenone, or FCCP.

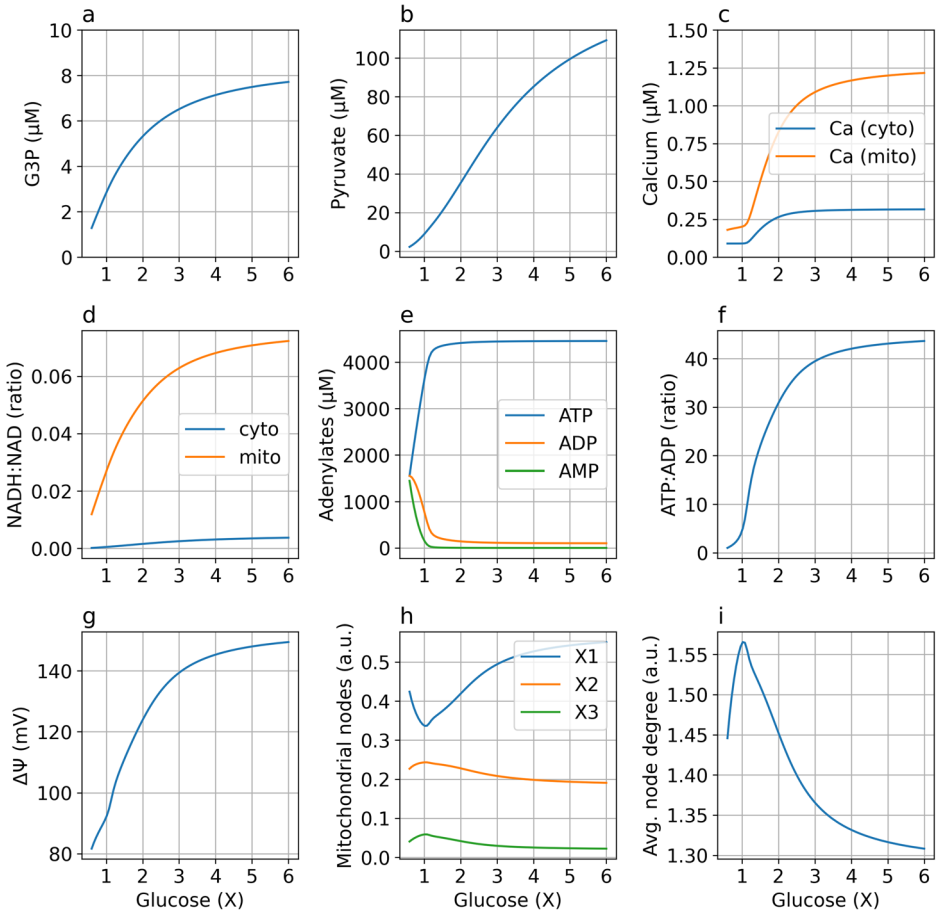

Fig. 3 | Simulated steady states under a range of glucose concentrations. Steady-state values of (**a**) glyceraldehyde 3-phosphate (in μM), (**b**) pyruvate (in μM), (**c**) calcium (in μM), (**d**) cytosolic and mitochondrial NADH-to-NAD ratios, (**e**) ATP, ADP, and AMP (in μM), (**f**) the ATP-to-ADP ratio, (**g**) the mitochondrial membrane potential (in millivolts, mV), (**h**) the mitochondrial population in node degrees 1, 2, and 3, and (**i**) the average degree of nodes were compared under different glucose concentrations. The x-axis represents relative glucose concentrations, with 5 mM being 1X in the model simulation.

Mitochondrial calcium (Fig. 3c) increased from calcium influx into the mitochondria through the mitochondrial calcium uniporter, further increasing the reaction rates of CAC and OXPHOS to produce more ATP. Our experimental measurement also showed that the ATP-to-ADP ratio increases with glucose (Supplementary Fig. 2a).

Moreover, the mitochondrial network became more fragmented in response to elevated glucose concentrations. The population of terminal degree-1 nodes (Fig. 3h) increased, while the average node degree decreased (Fig. 3i). The mitochondrial network showed the highest degree of fusion with the highest average degree of nodes at the resting glucose concentration (1X, 5 mM in the model).

Comparing microscopy images of INS-1 cells to model simulations

To corroborate the findings from our computational model, we obtained fluorescence microscopy images of INS-1 rat insulinoma cells under various metabolic conditions. We analyzed mitochondrial network morphologies under a range of glucose concentrations (0X, 1X, 3X, and 6X, where 1X represents 5 mM of glucose in the simulation and 2 g/L in the INS-1 experiments) (Fig. 4a–c) and mitochondrial toxicants: rotenone, oligomycin, and FCCP (Fig. 5a–c). The analysis of mitochondrial morphology revealed that the networks showed a greater degree of fusion at a baseline glucose concentration of 1X (5 mM) and were more fragmented when the glucose concentrations were high (3X, 6X) or low (0X) (Fig. 4d).

The fluorescence intensities of the membrane potential dependent tetramethylrhodamine methyl ester (TMRM) dye were the lowest at 0X, whereas higher values were obtained under 1X, 3X, and 6X glucose concentrations (Fig. 4d), revealing higher mitochondrial membrane potentials under higher glucose concentrations. A similar trend in mitochondrial membrane potential was also observed in the PANC-1 cell line stained with a fluorescent mitochondrion-specific dye and analyzed by flow cytometry (Supplementary Fig. 3).

Mitochondria treated with oligomycin exhibited the highest membrane potential, whereas those treated with FCCP had the lowest membrane potential (Fig. 5d). In addition, the membrane potential of the rotenone group was slightly lower than that of the control group, but the differences were not statistically significant. These results are consistent with the respective chemical mechanisms: oligomycin blocks ATP synthase, rotenone inhibits complex I in the ETC, and FCCP increases proton leak across the inner mitochondrial membrane.

With respect to mitochondrial morphology, the oligomycin group showed the most fragmented mitochondrial networks and rounded mitochondria (Fig. 5a). The FCCP group was less fragmented than the oligomycin group but more fragmented than the control group, although the low pixel intensity might impact the quality of the analysis. Compared with the control group, the rotenone group showed no significant change in mitochondrial morphology. The experimental and simulation results of galactose and free fatty acid addition showed more fused mitochondrial networks in the galactose group and more fragmented networks in the free fatty acid group. (Fig. 6, Supplementary Figs. 5, 6). Deoxyglucose, an analog of glucose that acts as a competitive inhibitor of glycolysis, is associated with mitochondrial fragmentation.

Prediction of the response to calcium oscillations

Cytosolic calcium is a key factor in the secretion of insulin by pancreatic cells. Mitochondria sense and shape cytosolic calcium in response to glucose stimulation to modulate metabolism–secretion coupling. An interesting topic that could be explored using our model is how mitochondria act as both recipients and generators of calcium signals. The following main types of cytosolic calcium oscillations have been observed in pancreatic β-cells:

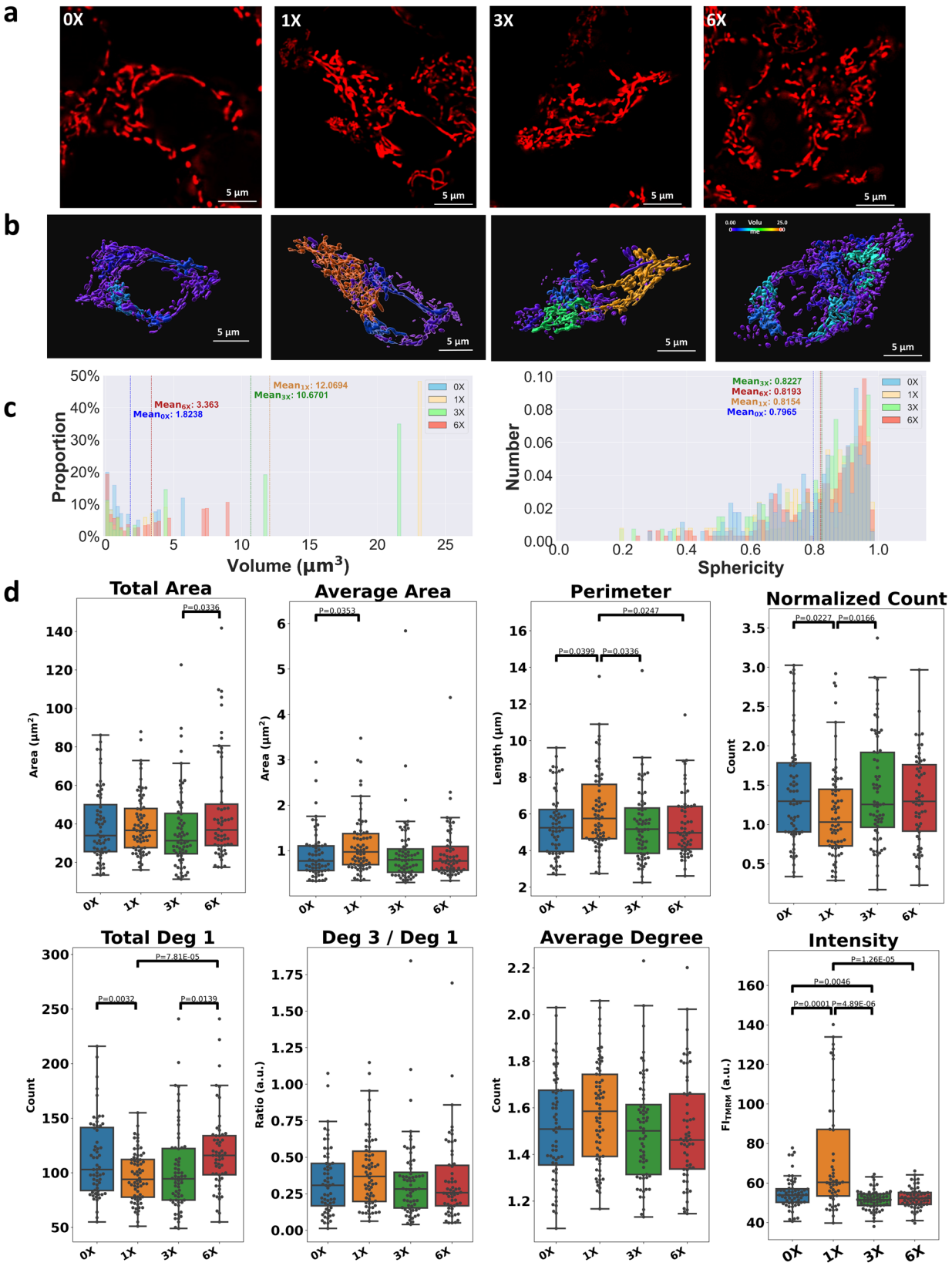

fast oscillations with periods ranging from seconds to slow oscillations with periods of minutes. In this study, we focused only on slow oscillations in pancreatic β-cells. The cytosolic calcium levels in our in silico model are steady-state averages controlled solely by the cytosolic ATP-to-ADP ratio without plasma membrane electrophysiology or calcium oscillations. Therefore, we introduced a periodic oscillator (see Eq. 10 in the supplementary note) of cytosolic calcium to investigate how our in silico model responds to cytosolic calcium oscillations[55]. The shape and period of the calcium oscillator were in accordance with previous studies[65] of mouse pancreatic β-cells under glucose stimulation (Fig. 6). Compared with the

Fig. 4 | Mitochondria in INS-1 cells exhibited distinct morphologies under different glucose concentrations. a Representative fluorescence images of mitochondria in INS-1 cells labeled with TMRM under our different glucose concentrations (with a baseline glucose concentration of 2 g/L, which is referred to as 1X in INS-1 cell culture medium). **b** Three-dimensional rendered surface images of the mitochondria in (**a**). The images were created using Imaris software (Oxford Instruments). The separated mitochondria are labeled with different colors corresponding to their volumes. **c** Histograms showing the distribution of volume and sphericity for separated mitochondrial components in an individual cell under a range of glucose concentrations. The data were acquired from cells in the images presented in (**a**). **d** Box plots of the 2D image analysis of mitochondria in INS-1 cells under different glucose concentrations. $N = 60$, 68, 64, and 58 cells for glucose concentrations of 0X, 1X, 3X, and 6X, respectively. The lower and upper bounds of the box are the first and third quartiles of the data, and the median is the line inside the box. The lower and upper whiskers represent the smallest and largest data points within 1.5 times the interquartile range from the first quartile and third quartile, respectively. All morphological indicator data were obtained using the image analysis pipeline in "Materials and Methods" section. Statistical significance was determined using Welch's *t* test.

cytosolic calcium levels, the mitochondrial calcium levels oscillated with a greater amplitude with a slight delay. However, the ATP-to-ADP ratio and the mitochondrial membrane potential decreased as the level of cytosolic calcium increased, due to increased calcium-dependent cytosolic ATP consumption, increasing ATP synthesis and export, and decreasing mitochondrial proton leakage. Accordingly, the mitochondrial network fused slightly during the surge of cytosolic calcium (Fig. 7).

Predicting the response of diabetic cells to glucose stimulation

To simulate the inhibition of mitochondrial metabolism in diabetic beta cells, we reduced the enzyme activities of pyruvate dehydrogenase, ETC complex, and ATP synthase[36] while increasing the rate of proton leakage[66] (Supplementary Table 1). Diabetes conditions were first tested by sequential challenges with glucose and chemicals (Fig. 8a–i) according to the experimental protocol used for mouse islets[36]. Compared to the baseline model, the diabetic model had lower cytosolic NADH levels but markedly higher pyruvate levels at higher glucose concentrations (Fig. 8k, l). The diabetic model also showed an attenuated response to increased glucose levels in terms of ATP levels, cytosolic and mitochondrial calcium levels, and mitochondrial membrane potential (Fig. 8e, f, g, h, n, o, p, q). Compared with the baseline model, the diabetic model presented higher mitochondrial NADH levels at lower glucose levels, but the baseline model showed higher mitochondrial NADH levels at higher glucose levels (Fig. 8m). Across various glucose levels, the change in mitochondrial network morphology was less prominent in the diabetic model than in the baseline model (Fig. 8r).

Comparison of glucose stimulation responses under various conditions

To summarize our findings, we plotted fission and fusion kinetics under glucose stimulation in different cellular conditions, including the default (baseline) model, the diabetic parameter set, the ETC inhibited by rotenone, the ATP synthase inhibited by oligomycin, and the proton leakage rate increased by FCCP (Fig. 9). The baseline model showed a biphasic response to glucose stimulation. The mitochondrial network was the most fused around the default glucose concentration of 5 mM (Fig. 9a, black line) because the fission force (related to the proton leakage rate) outpaced the fusion force (related to the ATP synthesis and export rate) at high glucose concentrations (Fig. 9b, black line). The simulations also showed that the mitochondrial networks were more fragmented than those in the baseline model in the presence of oligomycin and FCCP, as well as in the diabetic dataset.

Discussion

Mitochondria are highly dynamic and motile organelles that undergo constant fusion and fission, as observed from live-cell fluorescence imaging. These fission and fusion processes are critical for controlling the quality and function of mitochondria. An in silico model of mitochondrial bioenergetics and dynamics was proposed in this study, and this model reproduced several microscopic observations of pancreatic cell mitochondrial network morphology under various glucose concentrations and chemical treatments. Increasing the glucose concentration, inhibiting ATP synthase, and increasing proton leakage resulted in a fragmented mitochondrial network. The in silico approach provided the following insights into the driving forces of mitochondrial dynamics: the fission rate is related to proton leakage, and the fusion rate is associated with mitochondrial ATP synthesis and export.

Our in silico model was constructed based on two previous independent works that governed glucose-stimulated ATP synthesis and fission/fusion processes of mitochondrial networks[23,62]. The choice of fission/fusion rates connects cellular bioenergetics and mitochondrial dynamics together. For simplicity, we fixed the mitochondrial fission period to 10 min according to previous studies[35,59,63]. The fusion rate was increased by the OXPHOS ATP synthesis rate (J_{ANT}) and inhibited by the proton leakage rate (J_{HL}). These fission and fusion rates were then used to simulate the mitochondrial network architectures in bioimages under different modes of energy supply and expenditure. J_{ANT} and J_{HL} were chosen because uncoupling (proton leakage) can activate Oma1, which cleaves Opa1, to inhibit fusion. Uncoupling can also activate calcineurin and Drp1 to trigger fission[23,67]. In contrast, the GTP source for Opa1 may be fueled by mitochondrial ATP synthesis by ATP synthase and subsequent export by the adenine nucleotide translocator (ANT) and mitochondrial nucleoside diphosphate kinase (NDPK-D) at the inner mitochondrial membrane, promoting fusion and preventing mitophagy[68–71].

Because of the conservation of mass and charge, at steady state, the protons pumped by ETC complexes (J_{HR}) should balance protons return to mitochondria: either passing through ATP synthase (J_{HF}) to generate ATP or leaking through the inner mitochondrial membrane (J_{HL}). Proton flux through ATP synthase (J_{HF}) is also coupled to ATP export flux (J_{ANT}) at a ratio of 3:1 in our model. To summarize, at the steady state, the model has the following relationship:

$$J_{HR} = J_{HF} + J_{HL} = 3J_{ANT} + J_{HL} \quad (1)$$

A higher proton leakage rate (J_{HL}) relative to the ATP synthesis rate (J_{ANT}) results in more fragmented mitochondrial networks and a smaller average degree of mitochondrial nodes, and vice versa. High glucose concentrations increased the mitochondrial membrane potential ($\Delta\Psi m$) (Figs. 2, 3), $J_{ANT,}$ and J_{HL}. However, J_{HL} is exponentially dependent on $\Delta\Psi m$ and increases faster than J_{ANT}, which exhibits a sigmoidal dependence on $\Delta\Psi m$ (Fig. 9). Therefore, at higher glucose levels, the mitochondrial network was more fragmented, as indicated by a smaller average degree of nodes. The mitochondrial network also became more fragmented at glucose levels lower than the baseline value of 1X (5 mM) because a greater decrease was observed for J_{ANT} than J_{HL}. At the baseline glucose level (1X, 5 mM), the difference between the fusion and fission rates was greatest and the mitochondrial network was most fused. The inhibition of ATP synthase and increases in proton leakage resulted in a fragmented mitochondrial network. The model also reproduced the observed mitochondrial fragmentation (Fig. 4) after FCCP or oligomycin were added (Fig. 2) because the former enhances proton leakage (J_{HL}) and the latter inhibits ATP synthase (J_{ANT}) (Fig. 9). As simulated by a reduction in ETC activity in the ODE model, the addition of rotenone to block complex I hampered the response to glucose addition (Fig. 9) because the fission/fusion forces (J_{HL} and J_{ANT}) were both limited by the upstream reaction (J_{HR}). In our study, rotenone did not significantly change the mitochondrial network architecture, as shown by microscopy images of INS-1 cells (Fig. 5). However, the effects might depend on its dosage and cell type[72,73]. The mitochondrial network was tipped toward fusion when galactose was used as the culture medium and

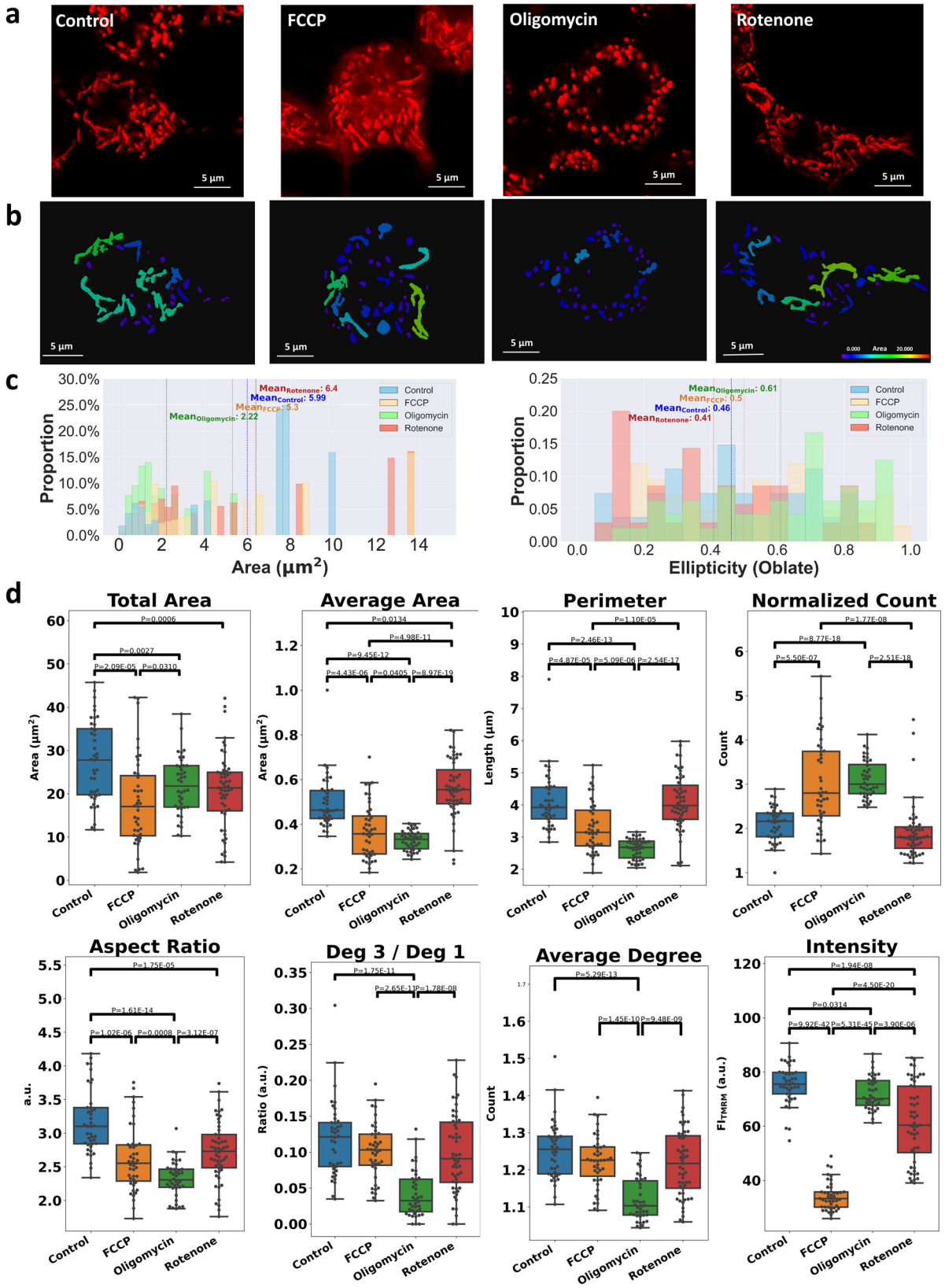

the cell were forced to utilize OXPHOS as the energy source, as demonstrated by the literature[74] and our experiments and simulations (Fig. 6 and Supplementary Fig. 5).

Overall, perturbations to mitochondrial energetics, such as increases in the proton leakage rate, inhibition of mitochondrial ATP synthase, and combined parameter alterations in diabetic cells, increased mitochondrial fragmentation. In contrast, inhibiting the ETC yielded a more fused mitochondrial network at high glucose concentrations because limiting proton pumping restricted J_{HL} more greatly than J_{ANT}. Compared with default parameters, perturbations to mitochondrial energetics parameters also

Fig. 5 | Mitochondria in INS-1 cells exhibited distinct morphologies under different chemical perturbations. a Representative fluorescence images of mitochondria in INS-1 cells labeled with TMRM in the presence of oligomycin, FCCP, and rotenone at a concentration of 10 μM. **b** Masked images of mitochondria in images (**a**). Binary images were first obtained using FIJI software and then mapped with different colors corresponding to their areas. **c** Histograms showing the distribution of area and ellipticity for separated mitochondrial components in an individual cell under different glucose concentrations. The data were acquired from cells in the images shown in (**b**). **d** Box plots of the 2D image analysis of mitochondria in INS-1 cells under different chemical conditions. $N = 41$, 43, 40, and 53 for the control, FCCP, oligomycin and rotenone groups, respectively. The lower and upper bounds of the box are the first and third quartiles of the data, and the median is the line inside the box. The lower and upper whiskers represent the smallest and largest data points within 1.5 times the interquartile range from the first quartile and third quartile, respectively. All morphological indicator data were obtained using the image analysis pipeline in "Materials and Methods" section. Statistical significance was determined using Welch's t test.

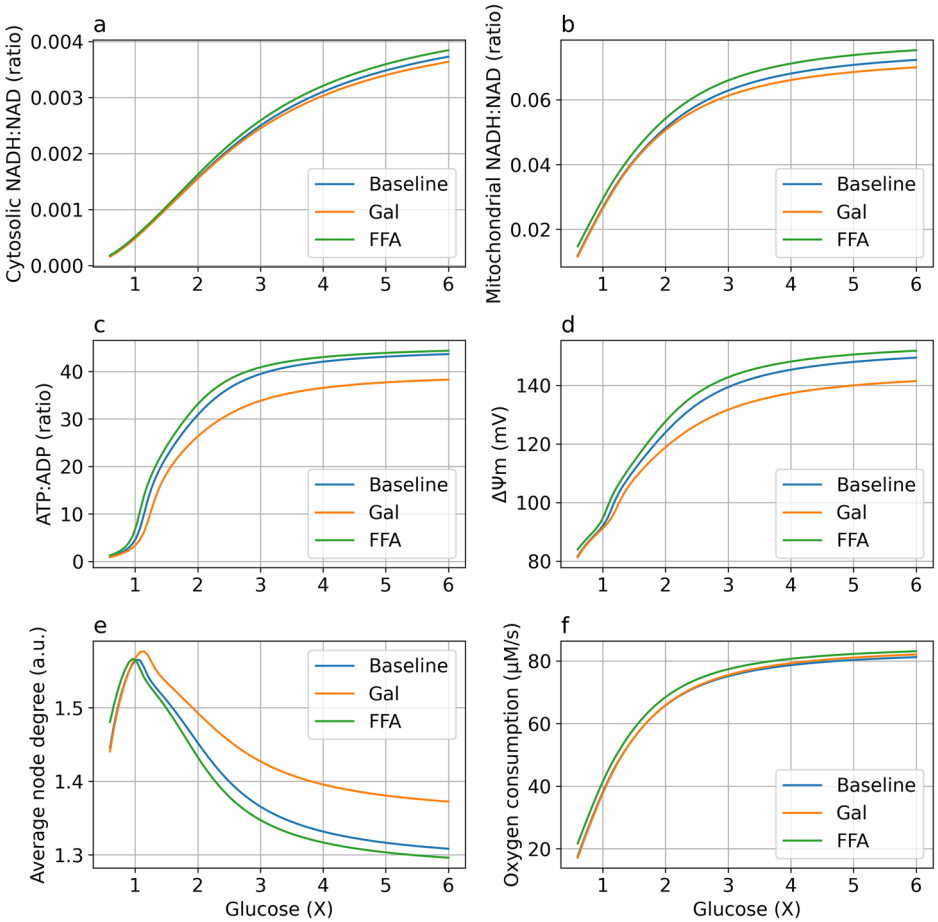

Fig. 6 | Comparison of baseline, galactose, and fatty acid addition models under a range of glucose/galactose levels. The steady-state values of (**a**) the cytosolic NADH-to-NAD ratio, (**b**) the mitochondrial NADH-to-NAD ratio, (**c**) the ATP-to-ADP ratio, (**d**) the mitochondrial membrane potential, (**e**) the average degree of the mitochondrial network, and (**f**) the oxygen consumption rate for the glucose parameters (blue, denoted Baseline), galactose model (orange, denoted Gal), and fatty acid addition (green, denoted FFA) across a range of glucose/galactose levels (with 1X equal to 5 mM).

reduced the dynamic range of fission/fusion rates across various glucose concentrations, which implied that the mitochondrial network structure is less responsive to metabolic changes. Our results also confirmed that the inhibition of mitochondrial fusion depends on the proton motive force and does not require the mitochondrial membrane potential to be reduced.

Mitochondrial dysfunction, including changes in respiratory chain activity, is related to dysfunctional GSIS in models of type 2 diabetes. Energy changes, such as reduced ATP levels, ATP-to-ADP ratios and mitochondrial membrane potential, were observed in diabetic beta-cells[75], and these cells exhibited increased levels of mitochondrial complex I, ATP synthase, uncoupler protein 2 (UCP-2), and reactive oxygen species (ROS)[76]. While mitochondrial dynamics maintain a metabolically efficient mitochondrial population, an imbalance between mitochondrial fusion and fission also contributes to beta-cell dysfunction in the progression of diabetes.

In the diabetic cell simulation, we reflected the inhibited mitochondrial metabolism in diabetic cells through restricting the activities of several metabolic checkpoints, including pyruvate dehydrogenase, which controls the CAC, the ETC, and ATP synthase[36]. In our simulations, the mitochondrial membrane potential and NADH levels were greater in the diabetic model than in the baseline model at a resting glucose concentration of 5 mM (Fig. 8m, p). However, the reverse was observed as the glucose concentration increased. This phenomenon was also observed by Haythorne et al.[36], who found that the restriction of mitochondrial metabolism blunted the responses to increasing glucose levels across various variables starting from the CAC, including mitochondrial calcium, NADH, and membrane potential. The limited ATP synthesis obtained from decreased ATP synthase activity and a lower mitochondrial membrane potential hampered the increases in the cytosolic ATP-to-ADP ratio and the cytosolic calcium levels (Fig. 8), reflecting the decreased effectiveness of insulin secretion in response to glucose stimulation. While we increased the basal proton leakage rate in the diabetic model in our simulation (Supplementary Table 1), the contribution of proton leakage to the total oxygen consumption rate (OCR) varied only slightly between healthy and diabetic mice (Fig. 8a), as observed in a previous study on mouse islets by Haythorne et al.[36]. The sensitivity to glucose stimulation in the ODE model mainly relies on the proton leakage rate[55]. A greater basal proton leakage rate shifted the curves of calcium and ATP responses rightwards (Fig. 8), decreasing the

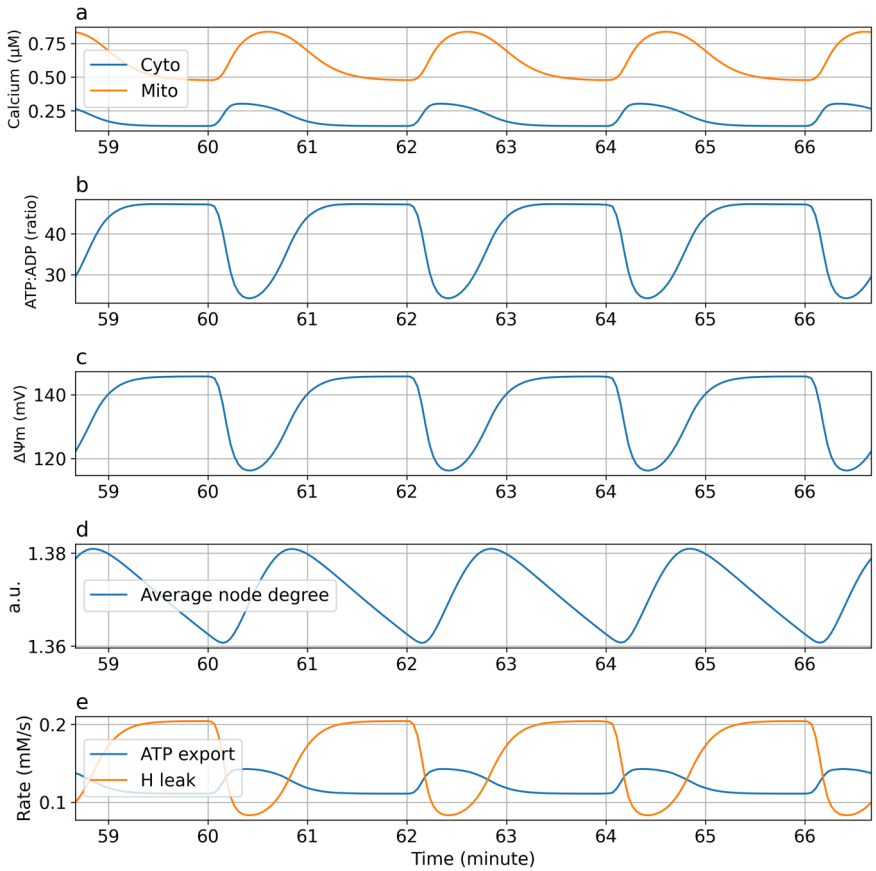

Fig. 7 | Response to cytosolic calcium oscillations. Cellular concentrations (in μM) of (**a**) cytosolic and mitochondrial calcium, (**b**) ATP-to-ADP ratio, (**c**) mitochondrial membrane potential (in mV), (**d**) the average degree of nodes in the mitochondrial network, and (**e**) the ATP export rate by the ANT and the proton leak rate. The results of the last 8 min of the simulation are shown.

responsiveness of the cells to glucose stimulation; this situation is more consistent with diabetic conditions, including persistent high glucose and lipid levels. Additionally, proton leakage across the inner mitochondrial membrane is mediated via uncoupler protein 2 (UCP-2), which is stimulated by high nutrient levels and ROS production and disrupts the mitochondrial membrane potential, ATP synthesis, and insulin secretion[66].

With respect to the mitochondrial network architecture, diabetic cells showed a more fragmented configuration than that of baseline cells in the model group at a resting glucose concentration of 5 mM, as the average degree of mitochondrial nodes was smaller (Fig. 8), which was consistent with previous microscopic observations[39,41,77]. The range for the average degree of mitochondrial nodes across various glucose concentrations was less prominent in the diabetic model than in the baseline model, possibly indicating that diabetic beta cells exhibit less metabolic plasticity than healthy beta cells (Figs. 8, 9)[22,67]. Aging also manifests as a metabolic syndrome characterized by impairments in glucose homeostasis, mitochondrial metabolism and insulin secretion from pancreatic β-cells. Our model might be able to explain the swelling and fragmented mitochondrial morphologies in aging cells[13,78].

To clarify the relationship between fusion/fission rates and environmental conditions, we adapted a graph theory-based network model[62] to simulate mitochondrial fission/fusion processes in individual mitochondria (Fig. 10). The network model consists of two types of fusion and fission events, tip-to-tip (C1) and tip-to-side (C2) fusion-to-fission ratios, to elongate and branch out the mitochondrial network. In our ODE model, the C1 and C2 fusion-to-fission ratios were influenced by the OXPHOS ATP synthesis rate and the proton leakage rate. Here, by observing C1 and C2, which were extracted and fitted to microscopy images from the mitochondrial network model, we estimated the propensity of different types of mitochondrial fusion and fission events under different conditions. In the case of low- to high-glucose conditions, mitochondria under 1X and 3X concentrations harbored greater amounts of C1 and C2 (Fig. 10d), which was consistent with the network-like morphologies observed from the image analysis. The lower values of C1 and C2 at 0X and 6X also corroborate the fragmented morphology of the mitochondria. In contrast, in the toxicity fitting, significantly fragmented mitochondria induced by oligomycin presented a lower C1 value. Higher C1 values were consistently found in the control group and in the group treated with rotenone between the image analysis results and the parameter fitting obtained from network modeling. Interestingly, the FCCP group had a lower C2 value rather than a lower C1 value. This result suggests that mitochondrial fragmentation by FCCP occurs through a different mechanism (decreased tip-to-side fusion) that does not involve oligomycin (decreased tip-to-tip fusion). By revisualizing the mitochondrial dynamics in the agent-based model simulation (Fig. 10f), "Average Degree" was tracked along with the iterations under different conditions (Fig. 10e), in which fragmented networks, such as those under oligomycin and 0X conditions, had smaller values during simulations. A simulated model for 1X glucose harbored the largest C1 and C2 and showed the most complicated network. In contrast, a simulated network for 0X was significantly fragmented with more segmented short branches, which was consistent with the results obtained through image analysis and genetic algorithm fitting. We also counted fission/fusion events in the time-lapse microscopy videos using a Mitometer[64] to confirm the simulation predictions. The ratios of fission-to-fusion rates (Supplementary Fig. 1) corresponded with the simulation results. The fission-to-fusion rates were lowest under the baseline glucose concentration (5 mM), and the ratio increased with low or high glucose levels and with oligomycin/FCCP treatment, corresponding to a more fragmented mitochondrial network.

All the models are abstractions to their real-world counterparts, and our ODE model is no exception. Our ODE model emphasizes the influence of mitochondrial bioenergetics on mitochondrial morphology. To easily constrain the parameters and analyze the general behavior of the model, we included some assumptions and simplifications.

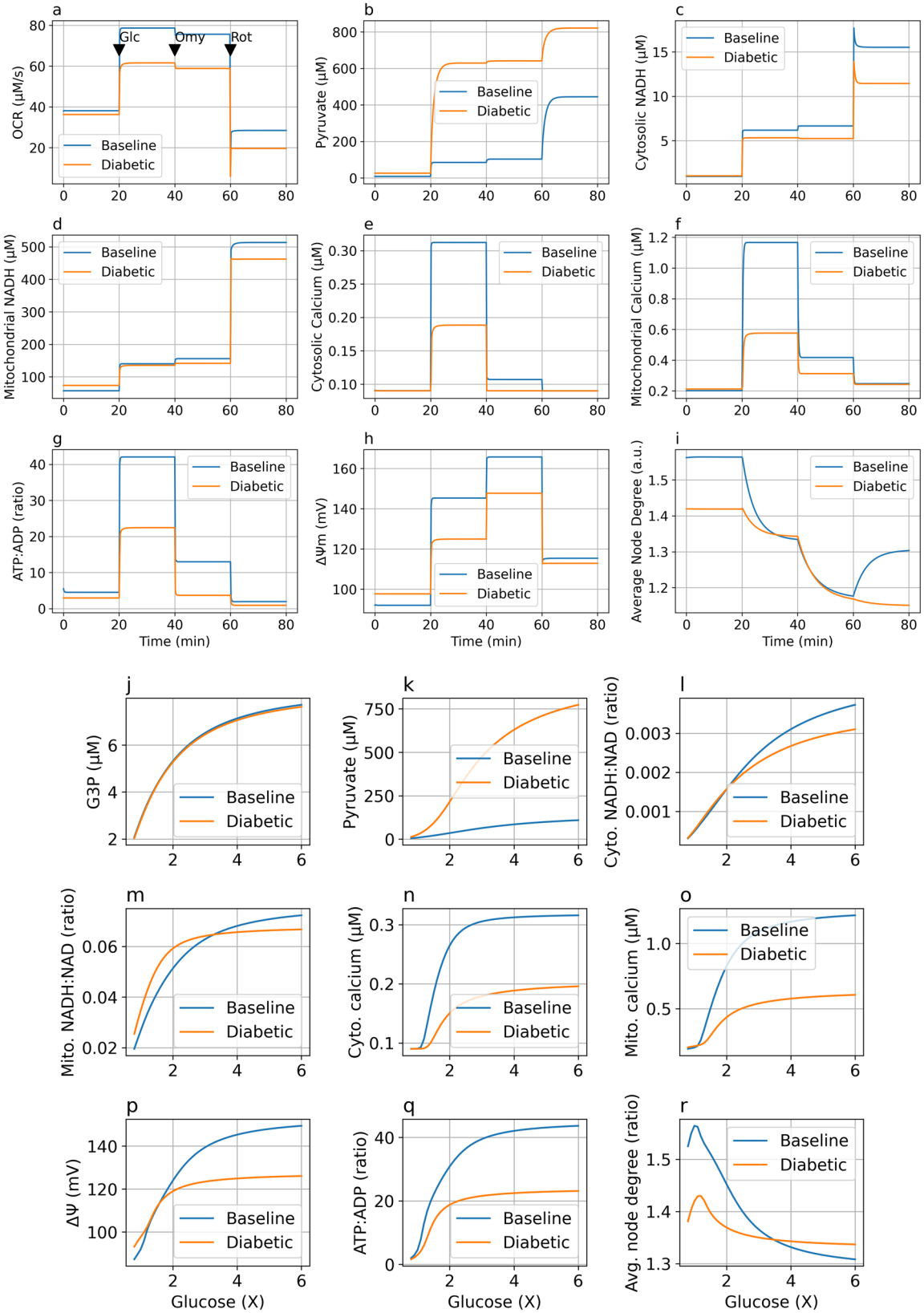

In our model, glucose served as the main energy source. Glycolysis and OXPHOS were the main metabolic pathways driving GSIS. Several metabolic pathways, such as the pentose phosphate pathway (PPP)[7,36], ROS generation and signaling[73,79], amino acid metabolism[33,36,40,80–82], lipid metabolism[40], and matrix mitochondrial GTP generation from the CAC, were not explicitly included in the model[70,83].

The cytosolic calcium levels in our model were calculated as steady-state averages as a function of the intracellular ATP-to-ADP ratio. As the focus of this study was the steady-state analysis of metabolic (ATP, mitochondrial membrane potential) implications for mitochondrial fission/fusion dynamics, a steady-state average cytosolic calcium level would facilitate the study of model behaviors. To avoid introducing too much

Fig. 8 | In silico ODE model response to glucose stimulation in the baseline and diabetic models. Panels (**a**)–(**i**): the (**a**) oxygen consumption rate (in μM/s), (**b**) pyruvate (in μM), (**c**) cytosolic NADH (in μM), (**d**) mitochondrial NADH (in μM), (**e**) cytosolic calcium (in μM), (**f**) mitochondrial calcium (in μM), (**g**) ATP-to-ADP ratio, (**h**) mitochondrial membrane potential (in mV), and (**i**) average degree of mitochondrial nodes are compared following the sequential addition of glucose and chemical reagents in the baseline and diabetic models. Initially, the glucose concentration is at a baseline of 5 mM. At t = 20 min, the glucose concentration is increased to 20 mM. At t = 40 min, ATP synthase activity is decreased by 90% to simulate the blockade of ATP synthase by oligomycin. At t = 60 min, the ETC capacity was decreased by 90% to simulate rotenone/antimycin A blocking respiratory complexes. The actions are indicated by arrows in the first panel (**a**) only. Panels (**j**)–(**r**): Steady-state values of (**j**) glyceraldehyde 3-phosphate, G3P (in μM), (**k**) pyruvate (in μM), (**l**) cytosolic NADH:NAD ratio, (**m**) mitochondrial NADH:NAD ratio, (**n**) cytosolic calcium (in μM), (**o**) mitochondrial calcium (in μM), (**p**) mitochondrial membrane potential (in mV), (**q**) ATP-to-ADP ratio, and (**r**) average degree of mitochondrial nodes are compared between baseline and diabetic models under different glucose concentrations. The relative glucose concentration of 5 mM is presented as 1X.

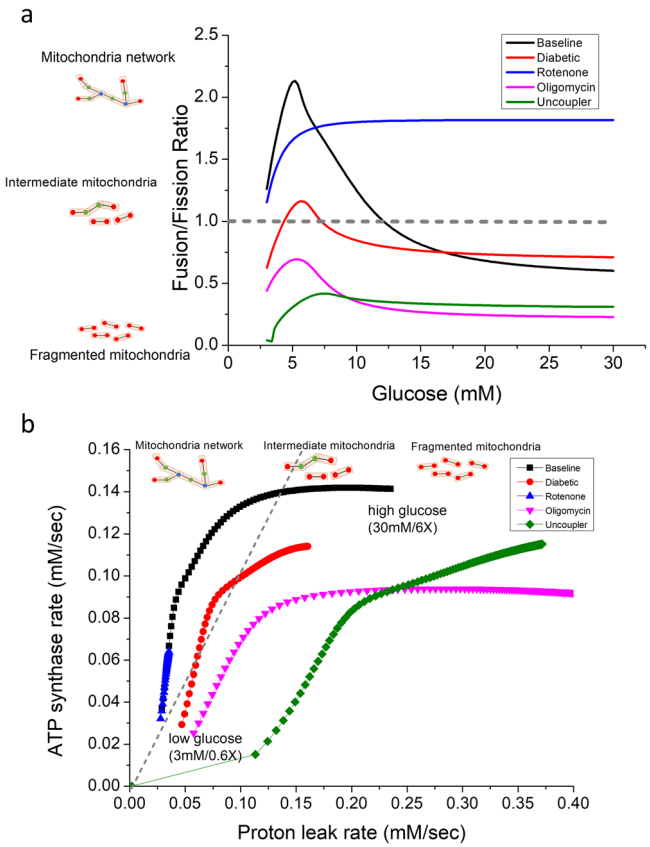

Fig. 9 | Effects of glucose stimulation under various conditions. a Ratios of the fusion to fission rates under the following conditions: default parameters (baseline, blue), diabetic parameters (diabetic, red), 90% ETC inhibition (rotenone, green), 90% ATP synthase inhibition (oligomycin, cyan), and five times the proton leakage rate (uncoupler, black). **b** Steady-state proton leakage rate (fission force) and ATP synthesis rate (fusion force) under various conditions (color codes are identical to **a**). Each dot represents the glucose concentration starting from 3 millimolar (the lower left dots) to 30 millimolar (the upper right dots) with an increment of 1 millimolar.

complexity into the model, the section representing calcium oscillations used an independent periodic function (Fig. 6 and "Materials and Methods") rather than including full descriptions of plasma membrane electrophysiology and calcium signaling[56,84,85]. This simple modeling could still reproduce the curves of cytosolic calcium and ATP levels in the previous beta-cell study[65]. The average degree of mitochondrial nodes fluctuated due to varying ATP synthesis rates and mitochondrial membrane potentials; however, the amplitude was smaller because the time scale of fission/fusion dynamics was substantially longer (10 min) than that of calcium oscillations (2 min). There are also reports that calcium overload is associated with mitochondrial fission[86,87]. This phenomenon was not observed in our model because calcium only performed a metabolic role and not a signaling role. Cytosolic calcium enhances cytosolic ATP consumption, and mitochondrial calcium enhances ATP synthase activity in our model. Thus, in the simulations, increasing calcium led to greater ATP synthase rates because more ADP was available due to cytosolic ATP consumption and a lower proton leak rate; this occurred because the proton motive force was tapped by ATP synthase. Therefore, the mitochondrial networks became more fused at higher calcium concentrations (Supplementary Fig. 7). However, calcium could increase mitochondrial fission when present at high calcium concentrations, particularly in the context of cellular stress, such as nutrient deprivation, as shown in the simulation.

In addition to ATP synthesis and proton leak flux, several bioenergetic mechanisms are involved in mitochondrial fusion/fission cycles. For instance, the fusion GTPase Opa1 is degraded in depolarized mitochondria to prevent damaged mitochondria from merging with the mitochondrial network[11]. Another component not included in this model was AMP-activated protein kinase (AMPK). During starvation, an increased AMP-to-ATP ratio activates AMP-activated protein kinase and triggers downstream signal transduction pathways to promote mitochondrial fission, mitophagy, and biogenesis[88–90]. However, mitochondrial mass was considered constant in our model without mitophagy or biogenesis processes. Additionally, the simulations focused on glucose levels higher than the baseline value of 5 mM; therefore, AMP-activated protein kinase activation via starvation played a lesser role in our simulations. Finally, mitochondrial network fragmentation is also associated with ROS[2,27,79,91]. However, because proton leakage and ROS generation increase with increasing mitochondrial membrane potential, the fission force, represented by proton leakage, can include mitochondrial fission events caused by ROS.

The mitochondria were assumed to be well mixed in our model with adequate fusion events[11,62]. As each mitochondrial node had the same metabolic profile, mitochondrial dynamics can be described by two ODEs. The average degree of nodes can represent the general trend of the mitochondrial network, whether it was fused or fragmented. However, an agent-based approach[35,59] is needed to trace individual mitochondria to monitor their health status and mitochondrial cluster formation. Each mitochondrion has at least three state variables (NADH, calcium, and the mitochondrial membrane potential) in the ODE model. The added complexity is beyond the scope of this study and could be investigated in future work.

Mitochondrial network organization and bioenergetic functions have bidirectional relationships[72]. Mitochondrial fission/fusion affects bioenergetic efficiency and energy expenditure, whereas mitochondrial morphology changes according to the cellular energy state. The metabolic signaling pathways AMP-activated protein kinase, insulin/IGF, and mTOR regulate mitochondrial dynamics for structural and functional adaptation. The bidirectional relationship and the detailed regulatory mechanisms should be further elucidated. Nonetheless, our simplified ODE model captured the changes in mitochondrial network morphology under different metabolic conditions and may serve as the basis for future works.

In conclusion, we devised a simple ODE-based mathematical model to bridge cellular bioenergetics and mitochondrial dynamics, and this model corroborated the behaviors based on fluorescence microscopy findings from INS-1 cells. The model also demonstrated that mitochondrial dynamics were regulated by ATP synthesis and proton leakage under various metabolic conditions. The mitochondrial networks were reconstructed in agent-based simulations that incorporated the fission/fusion rates from the model and image analysis. The combination of biophysical modeling and network analysis of experimental data can provide insights into the fundamental

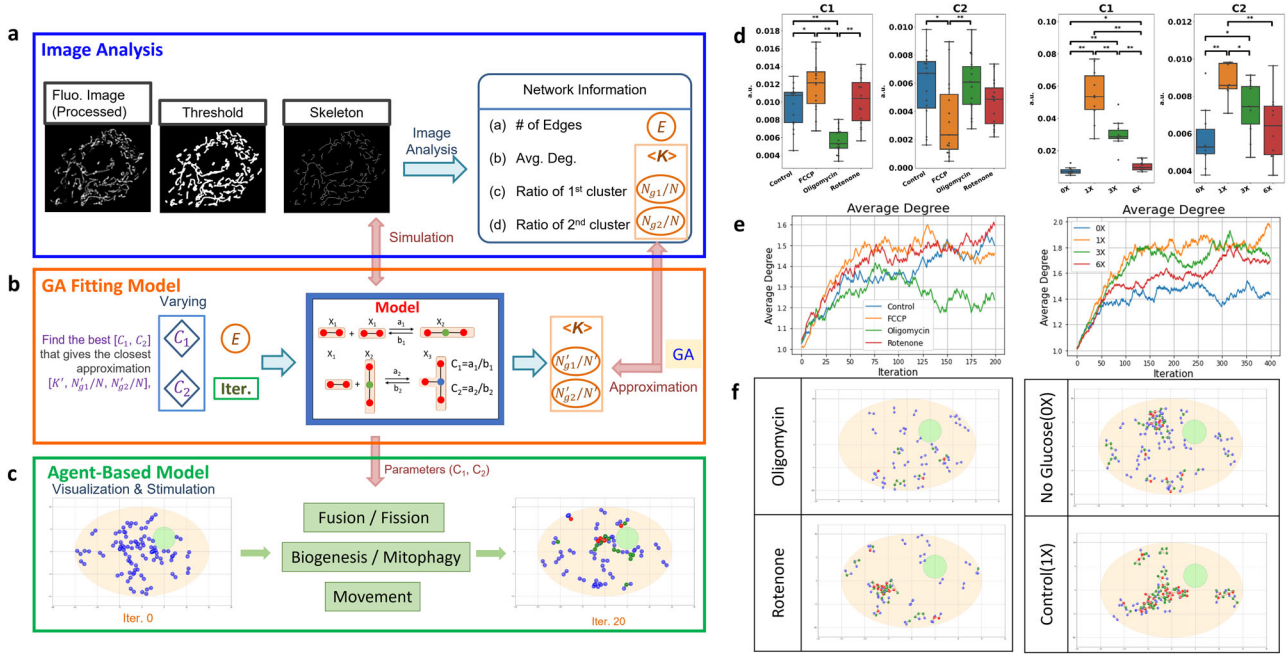

Fig. 10 | Workflow of mitochondrial network analysis and simulation. **a** Workflow of the mitochondrial network model simulation and fitting of fission/fusion rates. An agent-based mitochondrial network model simulating two types of fission and fusion behaviors using nodes, edges, and degrees is used to represent and describe the mitochondrial network. Edges are considered the basic units that represent small segments of mitochondria, and nodes with different degrees are regarded as characteristic measurements of the mitochondrial network structure. **b** Fitting fission/fusion rates of mitochondria under different glucose concentrations and chemical treatments. The network parameters <k> (average degree of mitochondrial nodes), Ng1/N (number of nodes or edges of the largest cluster/total nodes or edges), and Ng2/N (number of nodes or edges of the second largest cluster/total nodes or edges) were extracted from fluorescence images of INS-1 and used as features for genetic algorithm (GA) fittings. By minimizing the distance between the distribution of network parameters (D(<k>, Ng1/N, Ng2/N)) extracted from fluorescence image analysis and the network model, the optimized C1 (ratio of the rate constants of tip-to-tip fusion to tip-to-tip fission) and C2 (ratio of the rate constants of tip-to-side fusion to tip-to-side fission) were obtained by a random search of the GA. Kernel density estimation was used to estimate the probability density function of the network parameters from confocal microscopy images of mitochondria, and Kullback-Leibler divergence was used to minimize the difference between two distributions calculated from KDE. **c** Agent-based model for visualization of simulated mitochondrial networks with C1/C2 ratios obtained from GA. **d** Ten and fifteen repeats of fitting for glucose and toxicity 2D data, respectively. **e** Tracking indicator "average degree" of the simulated networks during the iterations. **f** Images of the mitochondrial network in the agent-based model.

principles underlying the complex processes by which organelle dynamics are regulated.

Materials and methods

In silico ODE model

Our computer simulation model (Supplementary Fig. 8) was built upon ten coupled ordinary differential equations (ODEs) (Supplementary Note 17) that integrate the bioenergetic and mitochondrial dynamics modules of the model[92]. The bioenergetic module was extended from the glucose-sensing beta-cell model by Fridlyand et al.[55]. The mitochondrial dynamics module was derived from the graph theory-based mitochondrial network model by Sukhorukov et al.[62].

The bioenergetic module described GSIS reactions, consisting of glycolysis, the CAC, OXPHOS, and calcium dynamics. First, glucose is metabolized to pyruvate via glycolysis. Pyruvate is then consumed in the mitochondria in the CAC to generate the reducing equivalents NADH and FADH2; these equivalents fuel ETC complexes to pump hydrogen ions out of mitochondria and thus create a voltage and pH difference across the inner mitochondrial membrane, which is known as the proton motive force. F1Fo-ATPase (ATP synthase) uses the proton motive force to synthesize ATP. An increase in the ATP-to-ADP ratio triggers calcium influx into the cytosol and then into the mitochondria via the mitochondrial calcium uniporter. An increase in the mitochondrial calcium concentration increases the CAC and OXPHOS reaction rates to generate more ATP from the mitochondria. The influx of calcium into the cytosol also triggers other biological processes, including the release of insulin-containing vesicles. Compared with the original work performed by Fridlyand et al.[55], we adjusted the mathematical expression of adenine nucleotide translocator (ANT) (Supplementary notes 11) and mitochondrial sodium-calcium exchanger[49,93] (Supplementary notes 15). We also added adenylate kinase (AdK) equilibria[94] to the cytosolic ATP-ADP-AMP pool (Supplementary notes 3). In this model, glucose was the main energy source[33,95].

The mitochondrial dynamics module describes the fission-fusion cycles of mitochondrial nodes and segments. The mitochondrial networks were represented by edges (mitochondrial mass) and nodes of degree 1 (end nodes), degree 2 (line segment nodes), and degree 3 (branching nodes). The fission/fusion cycle can be represented by the merging/splitting of nodes (Fig. 1). The mitochondrial fission rate was set to once every 10 min according to the literature[35], and the fusion rates were scaled from the ratio of the ATP synthase rate and the proton leakage rate[22]. This minimal model assumed that the mitochondria were evenly distributed and that their mass was conserved; thus, a population-based ODE model for degree-1, 2, and 3 nodes was used without tracking the movement and fission/fusion process of each individual mitochondrion.

At a resting glucose concentration of 5 mM (denoted as 1X), our in silico ODE model reached a steady state consistent with that of the original GSIS model (Supplementary Table 2), meaning our alterations to the ODE model did not induce marked deviations from the original model. The complete mathematical descriptions for the in silico model are described in the supplementary notes 1–19.

Computational environments. The in silico model was written in Julia[96] and was run on a workstation with an 8-core Xeon CPU. The ordinary differential equations (ODEs) were solved by the DifferentialEquations.jl[97]

and ModelingToolkit.jl[98] packages and were visualized by the PythonPlot.jl package, a Julia wrapper to the Python matplotlib[99] visualization package.

Steady-state values at various glucose concentrations. First, we obtained steady-state values of state variables under a 5 mM glucose concentration. The model was then simulated under a range of glucose concentrations from 3 mM to 30 mM until the model reached a steady state. We measured the influence of glycolytic flux on the steady-state levels of glyceraldehyde 3-phosphate, pyruvate, calcium, ATP, the mitochondrial membrane potential, the mitochondrial fission-fusion rates, and the state of the mitochondrial network.

Interactions between mitochondrial energetics and dynamics. To observe the interactions between mitochondrial energetics and dynamics, we paired a range of glucose concentrations with a range of one parameter (either ATP synthase activity, ETC complex activity, or proton leakage activity). The steady-state values of the average node degree, mitochondrial membrane potential, and ATP-to-ADP ratio were simulated for each combination.

Simulating galactose metabolism and free fatty acid addition. To simulate galactose metabolism instead of glucose metabolism, we increased the stoichiometry of ATP consumption for glucokinase (GK) from 2 to 4, because the conversion of galactose to glucose requires two ATP molecules. Thus, glycolysis yields zero ATP with galactose as the substrate.

To simulate free fatty acid addition, we introduced an additional mitochondrial NAD reduction pathway to model the beta oxidation pathway.

Response to calcium oscillations. The cytosolic calcium in Fridlyand's beta cell model represented average cytosolic calcium levels and was solely controlled by the cytosolic ATP-to-ADP ratio. When simulating oscillating calcium concentrations in stimulated beta cells (Fig. 7), cytosolic calcium kinetics were dependent on the cytosolic ATP-to-ADP ratios, and its concentrations were described by a time dependent, periodic function (Supplementary notes 8).

Simulating mitochondrial dynamics in diabetic cells. We investigated how diabetic beta cells react to glucose stimulation compared to healthy cells in terms of mitochondrial dynamics. We decreased the levels of pyruvate dehydrogenase, ETC, and ATP synthase and increased proton leakage to simulate metabolic changes in diabetic beta cells[36] (Supplementary Table 1). The steady-state values obtained from the baseline and diabetic settings were collected across a range of glucose levels from 3 mM (0.6X) to 30 mM (6.0X).

INS-1 cell culture. INS-1 cells (INS-1 832/13 rat insulinoma cell line, Sigma-Aldrich, SCC207) were cultured in RPMI-1640 (Sigma Cat. No. R0883) supplemented with 2 mM L-glutamine, 1 mM sodium pyruvate, 10 mM HEPES (Cat. No. TMS-003-C), and 0.05 mM β-mercaptoethanol + 10% FBS at 37 °C in the presence of 5% CO2 for 1 to 3 days before imaging.

For the glucose experiments, INS-1 cells were treated with glucose at concentrations of 0 g/L, 2 g/L, 6 g/L, and 12 g/L (Sigma, D8270) in RPMI1640 medium (Thermo Fisher Scientific, A2494201) for 5 min to represent the 0x, 1x, 3x, and 6x glucose groups, respectively. To assess the effects of palmitate on mitochondria, cells were exposed for 5 min to 1 mM palmitate complexed with BSA at a 6:1 ratio (Cayman Chemical, 29558) or to BSA alone (Sigma, A7030) as a control. Some treatment groups also included glucose. In additional experiments, INS-1 cells were cultured in RPMI1640 containing either 2 g/L glucose or 2 g/L galactose (Sigma, G5388), and glycolysis inhibition was induced by treating cells with RPMI1640 supplemented with 40 mM deoxyglucose (Sigma, D8357) for 1 h.

For the toxicity experiments, the culture media used were identical to those used in the glucose experiment. FCCP, oligomycin, and rotenone were added at a concentration of 10 μM. Microscopy images were taken immediately after FCCP was added, and in other cases, images were taken 30 min after the chemicals were added.

PANC-1 cell culture. PANC-1 cells (BCRC 60284) were cultured in DMEM (Corning, 10-013-CV) supplemented with 10% FBS. For confocal Airyscan imaging, cells were stained with TMRM (Tetramethylrhodamine, Methyl Ester) and then transferred to medium (Gibco, A1443001) containing different glucose concentrations (Sigma, D8270). The cells were incubated for 20-30 min at 37 °C to allow for equilibration. After incubation, confocal Airyscan imaging was performed to observe mitochondrial changes under the following glucose concentrations: 0 g/L (0X), 2.25 g/L (0.5X), 4.5 g/L (1X), and 9 g/L (2X).

Mitochondrial functional assays: ATP, NADH, ROS, and oxygen consumption assays

The ADP/ATP ratio was measured using the ADP/ATP Ratio Assay Kit (Abcam, ab65313). For this assay, 10,000 cells per well were seeded in a 96-well plate and incubated for 24 h prior to testing. The NAD/NADH ratio was determined using the NAD/NADH Assay Kit (Abcam, ab56348) with 2.5 × 10^6 cells cultured for 48 h in 35 mm dishes. To measure reactive oxygen species (ROS) levels, 3 × 10^4 cells were cultured for 72 h and analyzed using the Cellular ROS Assay Kit (Abcam, ab186027). All assays, including ATP/ADP, NADH/NAD, and ROS measurements, were performed using a SpectraMax iD3 microplate reader (Molecular Devices).

Microscopy image acquisition

Mitochondria were labeled with 100 nM TMRM and 100 nM nonyl acridine orange (NAO) for 15 min before imaging. A ZEISS LSM800 microscope with Airyscan and a 1.40 NA 63x objective lens was used for cell imaging. The software ZEN Blue 2.6 was utilized for fluorescent image acquisition and deconvolution.

Image preprocessing and thresholding. The image analysis pipeline used to obtain mitochondrial network morphology information was based on the study performed by Chaudhry et al.[43] using the ImageJ2 software (Supplementary Fig. 9). The inputs were TMRM or NAO fluorescence microscopy images of INS-1 cells. The pipeline comprised several preprocessing and analysis procedures. In the standard pipeline, input images are preprocessed by algorithms such as "Subtract Background" and "Enhanced Local Contract (CLAHE)" to denoise the images and enhance the contrast. After preprocessing, the images were binarized and skeletonized to analyze the mitochondrial network morphology and obtain mitochondrial features (Supplementary Table 3).

Mitochondrial membrane potential analysis. The TMRM fluorescence intensity is an indicator of the mitochondrial membrane potential. We quantified the average pixel intensities of each TMRM image using ImageJ to evaluate the changes in the membrane potential under different glucose concentrations and chemical environments. The mean value of the "Auto Threshold" values (obtained from FIJI) of the control group was set as the threshold. We considered only pixels with intensities larger than the threshold to prevent interference from background noise.

Mitochondrial network agent-based model

For the mitochondrial network model, a network with nodes and edges based on Sukhorukov's model[62] was used to simulate mitochondrial morphology, in which edges are regarded as mitochondria and nodes are regarded as locations where fusion and fission events occur[100]. In other words, the fusion and fission events of mitochondria are simulated by the connection and disconnection of edges, respectively. The simulation is then implemented by picking and performing one of the reactions from the two types of fusion and fission reactions (tip-to-tip and tip-to-side) mentioned

Table 1 | Propensities of mitochondrial node reactions

Mitochondrial node reactions	Equation	Propensity
tip-to-tip fusion	$X_1 + X_1 \xrightarrow{a_1} X_2$	$a_1(x_1)(x_1 - 1)$
tip-to-tip fission	$X_1 + X_1 \xleftarrow{b_1} X_2$	$b_1(x_2)$
tip-to-side fusion	$X_1 + X_2 \xrightarrow{a_2} X_3$	$a_2(x_1)(x_2)$
tip-to-side fission	$X_1 + X_2 \xleftarrow{b_2} X_3$	$b_2(x_3)$
tip-to-tip fission-fusion ratio	$c_1 = \frac{a_1}{b_1}$	
tip-to-side fission-fusion ratio	$c_2 = \frac{a_2}{b_2}$	

a_1, b_1, a_2, and b_2 are the rate constants of the reactions, and x_1, x_2, and x_3 are the numbers of nodes with degrees 1, 2, and 3, respectively. c1 and c2 are the ratios between the fusion and fission rates of the two reactions (tip-to-tip and tip-to-side). Reactions with a higher propensity have a greater probability of being chosen and performed.

iteratively. To decide which reaction to execute, the propensity of each reaction is calculated as in Table 1.

Finding the best fitted fission-fusion ratios in the mitochondrial network model to the static fluorescence images was the next task[41]. Three network parameters, <k> (average degree), Ng1/N (number of nodes or edges of the largest cluster divided by total nodes or edges) and Ng2/N (number of nodes or edges of the second largest cluster divided by total nodes or edges), were extracted from fluorescence images of INS-1 cells and used as features for the genetic algorithm. The same features were calculated using fitting from the simplified computational mitochondrial network model with 4 reactions. By adjusting parameters c1 and c2 in the simulations to vary the morphology of the final output network, we found the closest feature sets [<k'>, Ng1'/N', and Ng2'/N'] to the feature set [<k>, Ng1/N, and Ng2/N] obtained from image analysis. In other words, the feature set [<k>, Ng1/N, Ng2/N] can be extracted from both fluorescence images and network models, can act as a bridge between in vitro experiments and in silico model simulation, and provides an analytical and quantitative method to determine the fusion/fission rate-related parameters c1 and c2. To determine the difference between the feature sets, two statistical tools, kernel density estimation and Kullback–Leibler divergence, were utilized in this fitting model. In our cases, three one-variable probability density distributions D(<k>), D(Ng1/N) and D(Ng2/N) were estimated from several given samples of feature sets [<k>, Ng1/N, Ng2/N] using the python function "gaussian_kde" from the package scipy.stats. "Silverman's rule of thumb" was applied for bandwidth calculation using the built-in "scipy.stats.gaussian_kde" function for distribution estimations. The entropies between the probability distributions obtained from image analysis and the computational network model were then calculated by applying KLD to determine which feature set generated by network models (with different c1 and c2 as parameters) was the closest to the experimental data from image analysis during the fittings. The python function "entropy" from the package scipy.stats was applied for implementation. To find the optimal parameter set [c1, c2] that generated the best fit (i.e., gives the smallest entropy), a random search algorithm, the genetic algorithm, was applied using the open python package "geneticalgorithm" (available at https://pypi.org/project/geneticalgorithm/). The objective function that was minimized was set as the weighted average of the entropy of D(<k>), D(Ng1/N) and D(Ng2/N) between the simulation model and image analysis. Weights were set as [0.7, 0.15, 0.15] for [<k>, Ng1/N, Ng2/N] in INS-1 toxicity fitting and set as [0.45, 0.45, 0.1] in INS-1 glucose fitting, according to the levels of significant differences of each indicator among different conditions and trial and error.

Mitochondrial dynamics were then reconstructed and visualized in an agent-based model with the positions of nodes and edges of the mitochondrial network and events of fusion, fission, biogenesis, and mitophagy. In particular, the fission and fusion rates in the agent-based model were based on the parameters c1 and c2, which were obtained from the fitting previously and implemented to visualize mitochondrial dynamics in space and time. A total of 100 iterations were executed with 100 randomly located initialized nodes on a 30×30 (unit length^2) map. The locations of edges and nodes were restricted between the cell membrane and the nucleus.

Statistics and reproducibility. One-way ANOVA was performed to analyze the data from the glucose dose–response experiments. Welch's *t* test was applied to analyze the significant differences using the "ttest_ind" function from the "scipy" Python package. All the data presented as boxplots were plotted using the "boxplot" function provided in the "matplotlib" Python package. The lower and upper bounds of the box are the first (Q1) and third quartiles (Q3) of the data, respectively, and the median (Q2) is the line inside the box. The lower whisker extended to the smallest data point within 1.5 times the interquartile range below Q1 (i.e., Q1–1.5*(Q3-Q1)). The higher whisker extended to the largest data point within 1.5 times the interquartile range above Q3 (i.e., Q3 + 1.5*(Q3-Q1)). Statistical significance was shown if p value < 0.05. For the bar graphs, the error bars represent standard deviations.

Reporting summary

Further information on research design is available in the Nature Portfolio Reporting Summary linked to this article.

Data availability

The source data and images can be found at https://doi.org/10.5281/zenodo.13318372. All other data are available from the corresponding author upon reasonable request.

Code availability

The codes for the ODE model and agent-based model are available at https://doi.org/10.5281/zenodo.1330932192 and https://doi.org/10.5281/zenodo.13254168100.

Received: 2 December 2021; Accepted: 24 September 2024;
Published online: 05 October 2024

References

1. Tilokani, L., Nagashima, S., Paupe, V. & Prudent, J. Mitochondrial dynamics: Overview of molecular mechanisms. *Essays Biochem* **62**, 341–360 (2018).
2. Stiles, L. & Shirihai, O. S. Mitochondrial dynamics and morphology in beta-cells. *Best. Pract. Res. Clin. Endocrinol. Metab.* **26**, 725–738 (2012).
3. Fu, W., Liu, Y. & Yin, H. Mitochondrial dynamics: biogenesis, fission, fusion, and mitophagy in the regulation of stem cell behaviors. *Stem Cells Int* **2019**, 9757201 (2019).
4. Chan, D. C. Mitochondrial dynamics and its involvement in disease. *Annu. Rev. Pathol.* **15**, 235–259 (2020).
5. Bereiter-Hahn, J., Vöth, M., Mai, S. & Jendrach, M. Structural implications of mitochondrial dynamics. *Biotechnol. J.* **3**, 765–780 (2008).
6. Pickles, S., Vigié, P. & Youle, R. J. Mitophagy and quality control mechanisms in mitochondrial maintenance. *Curr. Biol.* **28**, R170–R185 (2018).
7. Montemurro, C. et al. Cell cycle-related metabolism and mitochondrial dynamics in a replication-competent pancreatic beta-cell line. *Cell Cycle* **16**, 2086–2099 (2017).
8. Pernas, L. & Scorrano, L. Mito-morphosis: Mitochondrial fusion, fission, and cristae remodeling as key mediators of cellular function. *Annu. Rev. Physiol.* **78**, 505–531 (2016).
9. Twig, G., Hyde, B. & Shirihai, O. S. Mitochondrial fusion, fission and autophagy as a quality control axis: The bioenergetic view. *Biochim. Biophys. Acta* **1777**, 1092–1097 (2008).
10. Molina, A. J. A. et al. Mitochondrial networking protects beta-cells from nutrient-induced apoptosis. *Diabetes* **58**, 2303–2315 (2009).

11. Mouli, P. K., Twig, G. & Shirihai, O. S. Frequency and selectivity of mitochondrial fusion are key to its quality maintenance function. *Biophys. J.* **96**, 3509–3518 (2009).
12. Alavi, M. V. & Fuhrmann, N. Dominant optic atrophy, OPA1, and mitochondrial quality control: understanding mitochondrial network dynamics. *Mol. Neurodegener.* **8**, 32 (2013).
13. Sharma, A., Smith, H. J., Yao, P. & Mair, W. B. Causal roles of mitochondrial dynamics in longevity and healthy aging. *EMBO Rep.* **20**, e48395 (2019).
14. Meyer, J. N., Leuthner, T. C. & Luz, A. L. Mitochondrial fusion, fission, and mitochondrial toxicity. *Toxicology* **391**, 42–53 (2017).
15. Youle, R. J. & van der Bliek, A. M. Mitochondrial fission, fusion, and stress. *Science* **337**, 1062–1065 (2012).
16. Song, Z., Ghochani, M., McCaffery, J. M., Frey, T. G. & Chan, D. C. Mitofusins and OPA1 mediate sequential steps in mitochondrial membrane fusion. *Mol. Biol. Cell* **20**, 3525–3532 (2009).
17. Song, Z., Chen, H., Fiket, M., Alexander, C. & Chan, D. C. OPA1 processing controls mitochondrial fusion and is regulated by mRNA splicing, membrane potential, and Yme1L. *J. Cell Biol.* **178**, 749–755 (2007).
18. Yu, R., Jin, S.-B., Lendahl, U., Nistér, M. & Zhao, J. Human Fis1 regulates mitochondrial dynamics through inhibition of the fusion machinery. *EMBO J.* **38**, e99748 (2019).
19. van der Bliek, A. M., Shen, Q. & Kawajiri, S. Mechanisms of mitochondrial fission and fusion. *Cold Spring Harb. Perspect. Biol.* **5**, a011072 (2013).
20. Smirnova, E., Griparic, L., Shurland, D. L. & van der Bliek, A. M. Dynamin-related protein Drp1 is required for mitochondrial division in mammalian cells. *Mol. Biol. Cell* **12**, 2245–2256 (2001).
21. Losón, O. C., Song, Z., Chen, H. & Chan, D. C. Fis1, Mff, MiD49, and MiD51 mediate Drp1 recruitment in mitochondrial fission. *Mol. Biol. Cell* **24**, 659–667 (2013).
22. Liesa, M. & Shirihai, O. S. Mitochondrial dynamics in the regulation of nutrient utilization and energy expenditure. *Cell Metab.* **17**, 491–506 (2013).
23. Mishra, P. & Chan, D. C. Metabolic regulation of mitochondrial dynamics. *J. Cell Biol.* **212**, 379–387 (2016).
24. Wai, T. & Langer, T. Mitochondrial dynamics and metabolic regulation. *Trends Endocrinol. Metab.* **27**, 105–117 (2016).
25. Dai, W. & Jiang, L. Dysregulated mitochondrial dynamics and metabolism in obesity, diabetes, and cancer. *Front Endocrinol. (Lausanne)* **10**, 570 (2019).
26. Glancy, B., Kim, Y., Katti, P. & Willingham, T. B. The functional impact of mitochondrial structure across subcellular scales. *Front. Physiol.* **11**, 541040 (2020).
27. Chen, H. & Chan, D. C. Mitochondrial dynamics in regulating the unique phenotypes of cancer and stem cells. *Cell Metab.* **26**, 39–48 (2017).
28. Ma, Y., Wang, L. & Jia, R. The role of mitochondrial dynamics in human cancers. *Am. J. Cancer Res.* **10**, 1278–1293 (2020).
29. Srinivasan, S., Guha, M., Kashina, A. & Avadhani, N. G. Mitochondrial dysfunction and mitochondrial dynamics-The cancer connection. *Biochim. Biophys. Acta Bioenerg.* **1858**, 602–614 (2017).
30. Kennedy, E. D. et al. Glucose-stimulated insulin secretion correlates with changes in mitochondrial and cytosolic Ca2+ in aequorin-expressing INS-1 cells. *J. Clin. Invest.* **98**, 2524–2538 (1996).
31. Wiederkehr, A. & Wollheim, C. B. Mitochondrial signals drive insulin secretion in the pancreatic β-cell. *Mol. Cell. Endocrinol.* **353**, 128–137 (2012).
32. Jhun, B. S., Lee, H., Jin, Z.-G. & Yoon, Y. Glucose stimulation induces dynamic change of mitochondrial morphology to promote insulin secretion in the insulinoma cell line INS-1E. *PLoS ONE* **8**, e60810 (2013).
33. Komatsu, M., Takei, M., Ishii, H. & Sato, Y. Glucose-stimulated insulin secretion: A newer perspective. *J. Diabetes Investig.* **4**, 511–516 (2013).
34. Schultz, J. et al. Precise expression of Fis1 is important for glucose responsiveness of beta cells. *J. Endocrinol.* **230**, 81–91 (2016).
35. Patel, P. K., Shirihai, O. & Huang, K. C. Optimal dynamics for quality control in spatially distributed mitochondrial networks. *PLoS Comput. Biol.* **9**, e1003108 (2013).
36. Haythorne, E. et al. Diabetes causes marked inhibition of mitochondrial metabolism in pancreatic β-cells. *Nat. Commun.* **10**, 2474 (2019).
37. Szendroedi, J., Phielix, E. & Roden, M. The role of mitochondria in insulin resistance and type 2 diabetes mellitus. *Nat. Rev. Endocrinol.* **8**, 92–103 (2011).
38. Panchal, K. & Tiwari, A. K. Mitochondrial dynamics, a key executioner in neurodegenerative diseases. *Mitochondrion* **47**, 151–173 (2019).
39. Rovira-Llopis, S. et al. Mitochondrial dynamics in type 2 diabetes: Pathophysiological implications. *Redox Biol.* **11**, 637–645 (2017).
40. Rutter, G. A., Georgiadou, E., Martinez-Sanchez, A. & Pullen, T. J. Metabolic and functional specialisations of the pancreatic beta cell: gene disallowance, mitochondrial metabolism and intercellular connectivity. *Diabetologia* **63**, 1990–1998 (2020).
41. Shah, S. I., Paine, J. G., Perez, C. & Ullah, G. Mitochondrial fragmentation and network architecture in degenerative diseases. *PLoS ONE* **14**, e0223014 (2019).
42. Supale, S., Li, N., Brun, T. & Maechler, P. Mitochondrial dysfunction in pancreatic β cells. *Trends Endocrinol. Metab.* **23**, 477–487 (2012).
43. Chaudhry, A., Shi, R. & Luciani, D. S. A pipeline for multidimensional confocal analysis of mitochondrial morphology, function, and dynamics in pancreatic β-cells. *Am. J. Physiol. Endocrinol. Metab.* **318**, E87–E101 (2020).
44. Lovy, A., Molina, A. J. A., Cerqueira, F. M., Trudeau, K. & Shirihai, O. S. A faster, high resolution, mtPA-GFP-based mitochondrial fusion assay acquiring kinetic data of multiple cells in parallel using confocal microscopy. *J. Vis. Exp*. e3991 https://doi.org/10.3791/3991 (2012)
45. Zhang, C.-L., Rodenkirch, L., Schultz, J. R. & Chiu, S. Y. A novel method to study the local mitochondrial fusion in myelinated axons in vivo. *J. Neurosci. Methods* **207**, 51–58 (2012).
46. Cortassa, S. & Aon, M. A. Computational modeling of mitochondrial function. *Methods Mol. Biol.* **810**, 311–326 (2012).
47. Cortassa, S., O'Rourke, B., Winslow, R. L. & Aon, M. A. Control and regulation of mitochondrial energetics in an integrated model of cardiomyocyte function. *Biophys. J.* **96**, 2466–2478 (2009).
48. Gauthier, L. D., Greenstein, J. L. & Winslow, R. L. Toward an integrative computational model of the Guinea pig cardiac myocyte. *Front. Physiol.* **3**, 244 (2012).
49. Nguyen, M.-H. T., Dudycha, S. J. & Jafri, M. S. Effect of Ca2+ on cardiac mitochondrial energy production is modulated by Na+ and H+ dynamics. *Am. J. Physiol., Cell Physiol.* **292**, C2004–C2020 (2007).
50. Wei, A.-C., Liu, T., Cortassa, S., Winslow, R. L. & O'Rourke, B. Mitochondrial Ca2+ influx and efflux rates in guinea pig cardiac mitochondria: low and high affinity effects of cyclosporine A. *Biochim. Biophys. Acta* **1813**, 1373–1381 (2011).
51. Zhou, L. et al. Modeling cardiac action potential shortening driven by oxidative stress-induced mitochondrial oscillations in guinea pig cardiomyocytes. *Biophys. J.* **97**, 1843–1852 (2009).
52. Magnus, G. & Keizer, J. Minimal model of beta-cell mitochondrial Ca2+ handling. *Am. J. Physiol.* **273**, C717–C733 (1997).
53. Bertram, R., Gram Pedersen, M., Luciani, D. S. & Sherman, A. A simplified model for mitochondrial ATP production. *J. Theor. Biol.* **243**, 575–586 (2006).

54. Saa, A. & Siqueira, K. M. Modeling the ATP production in mitochondria. *Bull. Math. Biol.* **75**, 1636–1651 (2013).
55. Fridlyand, L. E. & Philipson, L. H. Glucose sensing in the pancreatic beta cell: a computational systems analysis. *Theor. Biol. Med. Model.* **7**, 15 (2010).
56. Fridlyand, L. E., Tamarina, N. & Philipson, L. H. Bursting and calcium oscillations in pancreatic beta-cells: specific pacemakers for specific mechanisms. *Am. J. Physiol. Endocrinol. Metab.* **299**, E517–E532 (2010).
57. Fridlyand, L. E. & Philipson, L. H. Pancreatic beta cell G-protein coupled receptors and second messenger interactions: A systems biology computational analysis. *PLoS ONE* **11**, e0152869 (2016).
58. Fridlyand, L. E., Ma, L. & Philipson, L. H. Adenine nucleotide regulation in pancreatic beta-cells: modeling of ATP/ADP-Ca2+ interactions. *Am. J. Physiol. Endocrinol. Metab.* **289**, E839–E848 (2005).
59. Dalmasso, G., Marin Zapata, P. A., Brady, N. R. & Hamacher-Brady, A. Agent-based modeling of mitochondria links sub-cellular dynamics to cellular homeostasis and heterogeneity. *PLoS ONE* **12**, e0168198 (2017).
60. Hoffman, T. E., Barnett, K. J., Wallis, L. & Hanneman, W. H. A multimethod computational simulation approach for investigating mitochondrial dynamics and dysfunction in degenerative aging. *Aging Cell* **16**, 1244–1255 (2017).
61. Tam, Z. Y., Gruber, J., Halliwell, B. & Gunawan, R. Mathematical modeling of the role of mitochondrial fusion and fission in mitochondrial DNA maintenance. *PLoS ONE* **8**, e76230 (2013).
62. Sukhorukov, V. M., Dikov, D., Reichert, A. S. & Meyer-Hermann, M. Emergence of the mitochondrial reticulum from fission and fusion dynamics. *PLoS Comput. Biol.* **8**, e1002745 (2012).
63. Kornick, K., Bogner, B., Sutter, L. & Das, M. Population dynamics of mitochondria in cells: A minimal mathematical model. *Front. Phys*. **7**, 146 (2019).
64. Lefebvre, A. E. Y. T., Ma, D., Kessenbrock, K., Lawson, D. A. & Digman, M. A. Automated segmentation and tracking of mitochondria in live-cell time-lapse images. *Nat. Methods* **18**, 1091–1102 (2021).
65. Gregg, T. et al. Pancreatic β-cells from mice offset age-associated mitochondrial deficiency with reduced KATP channel activity. *Diabetes* **65**, 2700–2710 (2016).
66. Lowell, B. B. & Shulman, G. I. Mitochondrial dysfunction and type 2 diabetes. *Science* **307**, 384–387 (2005).
67. Liesa, M., Palacín, M. & Zorzano, A. Mitochondrial dynamics in mammalian health and disease. *Physiol. Rev.* **89**, 799–845 (2009).
68. Boissan, M. et al. Membrane trafficking. Nucleoside diphosphate kinases fuel dynamin superfamily proteins with GTP for membrane remodeling. *Science* **344**, 1510–1515 (2014).
69. Lacombe, M.-L., Tokarska-Schlattner, M., Boissan, M. & Schlattner, U. The mitochondrial nucleoside diphosphate kinase (NDPK-D/NME4), a moonlighting protein for cell homeostasis. *Lab. Invest.* **98**, 582–588 (2018).
70. Tokarska-Schlattner, M. et al. The nucleoside diphosphate kinase D (NM23-H4) binds the inner mitochondrial membrane with high affinity to cardiolipin and couples nucleotide transfer with respiration. *J. Biol. Chem.* **283**, 26198–26207 (2008).
71. Schlattner, U. et al. NME4/nucleoside diphosphate kinase D in cardiolipin signaling and mitophagy. *Lab. Invest.* **98**, 228–232 (2018).
72. Benard, G. et al. Mitochondrial bioenergetics and structural network organization. *J. Cell Sci.* **120**, 838–848 (2007).
73. Koopman, W. J. H. et al. Inhibition of complex I of the electron transport chain causes O2-. -mediated mitochondrial outgrowth. *Am. J. Physiol., Cell Physiol.* **288**, C1440–C1450 (2005).
74. Shiratori, R. et al. Glycolytic suppression dramatically changes the intracellular metabolic profile of multiple cancer cell lines in a mitochondrial metabolism-dependent manner. *Sci. Rep.* **9**, 18699 (2019).
75. Anello, M. et al. Functional and morphological alterations of mitochondria in pancreatic beta cells from type 2 diabetic patients. *Diabetologia* **48**, 282–289 (2005).
76. Sivitz, W. I. & Yorek, M. A. Mitochondrial dysfunction in diabetes: from molecular mechanisms to functional significance and therapeutic opportunities. *Antioxid. Redox Signal.* **12**, 537–577 (2010).
77. Dlasková, A. et al. 4Pi microscopy reveals an impaired three-dimensional mitochondrial network of pancreatic islet beta-cells, an experimental model of type-2 diabetes. *Biochim. Biophys. Acta* **1797**, 1327–1341 (2010).
78. Amartuvshin, O. et al. Aging shifts mitochondrial dynamics toward fission to promote germline stem cell loss. *Aging Cell* **19**, e13191 (2020).
79. Yu, T., Robotham, J. L. & Yoon, Y. Increased production of reactive oxygen species in hyperglycemic conditions requires dynamic change of mitochondrial morphology. *Proc. Natl Acad. Sci. USA* **103**, 2653–2658 (2006).
80. Lien, E. C. & Vander Heiden, M. G. Pancreatic β cells put the glutamine engine in reverse. *Cell Metab.* **33**, 702–704 (2021).
81. Stark, R. & Kibbey, R. G. The mitochondrial isoform of phosphoenolpyruvate carboxykinase (PEPCK-M) and glucose homeostasis: has it been overlooked? *Biochim. Biophys. Acta* **1840**, 1313–1330 (2014).
82. Zhang, G.-F. et al. Reductive TCA cycle metabolism fuels glutamine- and glucose-stimulated insulin secretion. *Cell Metab.* **33**, 804–817.e5 (2021).
83. Jesinkey, S. R. et al. Mitochondrial GTP links nutrient sensing to β cell health, mitochondrial morphology, and insulin secretion independent of oxphos. *Cell Rep.* **28**, 759–772.e10 (2019).
84. Bertram, R., Sherman, A. & Satin, L. S. Electrical, calcium, and metabolic oscillations in pancreatic islets. in *Islets of Langerhans* (ed. Islam, Md. S.) 453–474 (Springer Netherlands). :https://doi.org/10.1007/978-94-007-6686-0_10 2015
85. Klec, C., Ziomek, G., Pichler, M., Malli, R. & Graier, W. F. Calcium signaling in ß-cell physiology and pathology: A revisit. *Int. J. Mol. Sci*. **20**, 6110 (2019).
86. Kaddour-Djebbar, I. et al. Specific mitochondrial calcium overload induces mitochondrial fission in prostate cancer cells. *Int. J. Oncol.* **36**, 1437–1444 (2010).
87. Zhou, X. et al. Mitochondrial dynamics: A potential therapeutic target for ischemic stroke. *Front. Aging Neurosci.* **13**, 721428 (2021).
88. Curry, D. W., Stutz, B., Andrews, Z. B. & Elsworth, J. D. Targeting AMPK signaling as a neuroprotective strategy in parkinson's disease. *J. Parkinsons Dis.* **8**, 161–181 (2018).
89. Lin, S.-C. & Hardie, D. G. AMPK: Sensing glucose as well as cellular energy status. *Cell Metab.* **27**, 299–313 (2018).
90. Toyama, E. Q. et al. Metabolism. AMP-activated protein kinase mediates mitochondrial fission in response to energy stress. *Science* **351**, 275–281 (2016).
91. Khacho, M. et al. Mitochondrial dynamics impacts stem cell identity and fate decisions by regulating a nuclear transcriptional program. *Cell Stem Cell* **19**, 232–247 (2016).
92. Tseng, W.-W. ntumitolab/mitodyn-ode: 20240813. *Zenodo* https://doi.org/10.5281/zenodo.13309321 (2024).
93. Dash, R. K. & Beard, D. A. Analysis of cardiac mitochondrial Na + -Ca2+ exchanger kinetics with a biophysical model of mitochondrial Ca2+ handling suggests a 3:1 stoichiometry. *J. Physiol. (Lond.)* **586**, 3267–3285 (2008).
94. Golding, E. M., Teague, W. E. & Dobson, G. P. Adjustment of K' to varying pH and pMg for the creatine kinase, adenylate kinase and

ATP hydrolysis equilibria permitting quantitative bioenergetic assessment. *J. Exp. Biol.* **198**, 1775–1782 (1995).
95. Nicholls, D. G. The pancreatic β-cell: A bioenergetic perspective. *Physiol. Rev.* **96**, 1385–1447 (2016).
96. Bezanson, J., Edelman, A., Karpinski, S. & Shah, V. B. Julia: A fresh approach to numerical computing. *SIAM Rev*. **59**, 65–98 (2017).
97. Rackauckas, C. & Nie, Q. DifferentialEquations.jl – A performant and feature-rich ecosystem for solving differential equations in Julia. *J. Open Res. Softw*. **5**, (2017).
98. Ma, Y. et al. ModelingToolkit: A composable graph transformation system for equation-based modeling. *arXiv* https://doi.org/10.48550/arxiv.2103.05244 (2021).
99. Hunter, J. D. Matplotlib: A 2D graphics environment. *Comput. Sci. Eng.* **9**, 90–95 (2007).
100. Tseng, W.-W. ntumitolab/Mitochondrial-Network-Model: 20240807. *Zenodo* https://doi.org/10.5281/zenodo.13254168 (2024).

Acknowledgements

We thank the National Center for High-performance Computing (NCHC) in Taiwan for providing computational and storage resources. This work was supported by grants from the Ministry of Science and Technology in Taiwan (MOST-109-2636-B-002-001 and MOST-110-2636-B-002-017 to AW), grant from the National Taiwan University Center for Advanced Computing and Imaging in Biomedicine (NTU-112L900701 to AW), grant from the National Health Research Institutes in Taiwan (NHRI-EX-113-11121SC to AW), and grants from the Research Grants Council of the Hong Kong Special Administrative Region, China (Project #: CUHK 14219922 and C5005-23W to YH) and the VC Discretionary Fund, the Chinese University of Hong Kong (Project #: 8601014 to YH).

Author contributions

A.-C. W. and W.-W. T. contributed to designing the study. W.-W. T., C.-H. C., and C. C. constructed the models and performed model simulations. Y.-J. L and S. Z. performed the experiments and analyzed the experimental data. C.-H. C. performed image analysis. W.-W. T., C.-H. C., and A.-C. W. wrote the manuscript. W.-W. T., Y-P. H. and A.-C. W. revised the manuscript based on comments from all reviewers. All authors read and approved the final manuscript.

Competing interests

The authors declare no competing interests.

Additional information

Supplementary information The online version contains supplementary material available at https://doi.org/10.1038/s42003-024-06955-3.

Correspondence and requests for materials should be addressed to An-Chi Wei.

Peer review information *Communications Biology* thanks Ghanim Ullah and the other, anonymous, reviewer(s) for their contribution to the peer review of this work. Primary Handling Editors: Gene Chong and Laura Rodríguez Pérez. A peer review file is available.